Journal of Nanotechnology

Application and Characterization of Nanomaterials for Industrial and Environmental Processes

Lead Guest Editor: Giorgio Vilardi
Guest Editors: Vu Duc Chinh, Javier M. Ochando-Pulido, and Maria Paola Bracciale

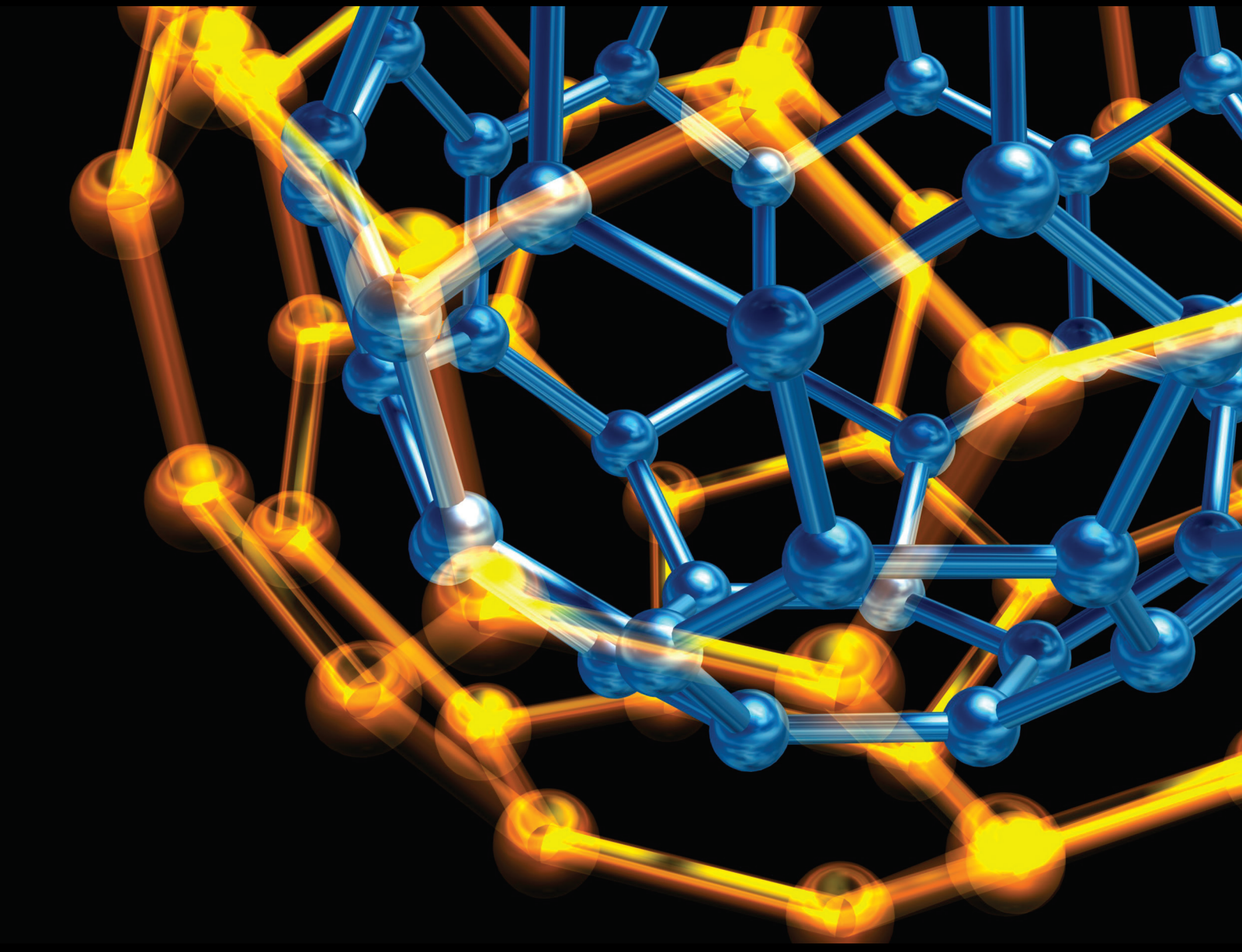

Application and Characterization of Nanomaterials for Industrial and Environmental Processes

Journal of Nanotechnology

Application and Characterization of Nanomaterials for Industrial and Environmental Processes

Lead Guest Editor: Giorgio Vilardi
Guest Editors: Vu Duc Chinh, Javier M. Ochando-Pulido, and Maria Paola Bracciale

Contents

Hindawi
Journal of Nanotechnology
Volume 2020, Article ID 8147080, 8 pages
https://doi.org/10.1155/2020/8147080

Review Article

Nanoparticle Therapy Is a Promising Approach in the Management and Prevention of Many Diseases: Does It Help in Curing Alzheimer Disease?

Lamyaa M. Kassem,[1] **Nada A. Ibrahim**,[1] **and S. Ayesha Farhana**[2]

[1]*Department of Pharmacy Practice, Unaizah College of Pharmacy, Qassim University, P.O. Box: 5888, Unaizah 51911, Qassim, Saudi Arabia*
[2]*Department of Pharmaceutics, Unaizah College of Pharmacy, Qassim University, Unaizah, Qassim, Saudi Arabia P.O. Box: 5888*

Correspondence should be addressed to Lamyaa M. Kassem; abdo.200312@yahoo.com

Received 20 September 2019; Accepted 6 June 2020; Published 7 August 2020

Guest Editor: Giorgio Vilardi

Treatment of brain diseases is always limited by the physiological nature of the highly selective blood-brain barrier (BBB) and the electrostatic charge of the nanoporous extracellular matrix. Nanomedical application provides a promising drug delivery revolution for the treatment of neurodegenerative diseases (NDDs). It depends on improving the pharmacokinetic distribution of drugs through the central nervous system. Nanotechnology offers various forms of nanoparticles, and these nanoparticles have brain-targeted and long-acting properties with minimal systemic adverse effects and motor complications. Gene delivery vehicles and nanocarriers including neurotrophic factors are promising therapeutics for many NDDs, and they can modulate neuronal survival and synaptic connectivity. Neurotrophic factors when integrated with the nanotechnological approaches can pass the BBB merely, representing a significant challenging track. Clinical trials proved that levodopa nanoparticles cause little motor complications which is a considerable drawback in treating Parkinson's disease with levodopa. Recently, nanotechnology had patented new formulations and achieved various advanced procedures for management, and even prevention, of NDDs. Nanotechnology can be integrated into neuroscience to fight against neurodegenerative diseases. Primary research studies in using nanoparticles to cure Alzheimer disease (AD) are promising but are still in need for more investigations. The present paper aims to review, outline, and summarize various efforts done in the field of using nanoparticles in the management of Alzheimer.

1. Introduction to Neurodegenerative Diseases and Nanoparticles

Neurodegenerative diseases (NDDs) are debilitating disorders that primarily affect the neuron cells, and they degenerate the brain and central nervous system (CNS) progressively which severely disturb the motor and cognitive functions which may end with either complete disabilities or death. Symptoms of NDDs often progress slowly over the years [1]. The resulting short- or long-term impairments and limitations may burden the quality of life of patients, families, and social networks [2]. NDDs are of different types such as Alzheimer's disease (AD), Parkinson's disease (PD), dementia, motor neuron diseases (MND), Huntington's disease (HD), prion disease, and schizophrenia. In this review, we will focus on challenging experimental and clinical trials in the treatment of the AD as one of the most common NDDs among elders. Despite the variations in clinical characteristics, there are some molecular and subcellular similarities between these NDDs. NDDs have standard features which include a late appearance in life, synaptic abnormalities, extensive neuronal loss, and gathering and collection of protein within the brain [3]. Millions of people globally may have dementia mainly due to AD, which causes an irreversible type. It occurs in nearly 1% of the individuals in the age of

more than 50 yrs and may jump to 50% in adults more than 70 yrs [4]. Profoundly, these percentages are expected to increase with the worldwide increase in the population mean age. AD is a chronic NDD, and it is considered as a leading cause of dementia in elders; the causative mechanisms of the AD are still unclear. The amyloid beta peptide protein plaques are deposited extracellularly around the walls of cerebral vessels and in the brain parenchyma [5]. They degenerate a person's physical and mental skills during their prime working years and has no cure [6]. In this review, we aim to review, outline, and summarize various efforts done in the field of using nanoparticles in the management of Alzheimer.

Various fields of sciences were interested in using this era of nanotechnology in challenges in the treatment and diagnosis of NDDs, see Figure 1 which reflects 236 published papers since 1994 of different fields of science with years of citations as provided by the Web of Science search result analysis [7].

The BBB has a nature of specific permeability which represents the main challenge in the treatment of NDDs. The challenge is either to manipulate the drug in a ridiculously small size that can easily pass the cells of the BBB or to change the physicochemical parameters of the drug in a way that it will be lipid soluble. All the available CNS treatment medications can hardly penetrate the BBB to give the required therapeutic effect in the brain and CNS. Considerable research studies indicate that enhancing the permeability and bioavailability of the BBB is needed to improve therapeutic outcomes. Nanotechnology medical applications offer many new promising opportunities for efficient brain drug delivery across the BBB that we will outline throughout the review [8].

Nanoparticle systems can be used with several routes of administration such as oral [9], nasal [10], and parenteral including intravenous [11], intramuscular [12], subcutaneous [13], and intraocular [14]. The majority of the nanoparticle systems that are used are composed of both natural and synthetic polymers, proteins, and polysaccharides in which the drug is incorporated for targeted brain delivery [15]. These polymeric nanoparticles have promising brain-targeting characters as modifiable chemical characters for cell-specific and selective targeting purposes and the ability to change the drug-releasing pattern for controlled, sustained, or extended drug effects, shielding the in situ drug in a way that interferes with the lipophilic requirement to pass the BBB, which can also protect the drug from the enzymatic degradation or the first-pass metabolism effects, which all can help to increase the bioavailability, decrease the required therapeutic dose, and hence decrease the drug toxicity and systemic adverse effects. The size of the nanoparticle systems ranges from 1 to 1000 nm. There are many forms of nanosystems such as nanoparticles, nanocapsules, nanospheres, nanogels, nanosuspensions, nanomicelles, and nanoliposomes. The choice of a proper type of nanosystem depends on the nature of the targeted cell or location, the nature and mass of the drug, the required pattern of drug release, type of the dosage form, and, in general, the nature of the drug challenge to reach the brain or CNS [16].

2. Advantages of Using Nanoparticles for CNS-Targeted Drug Delivery

In general, nanoparticles offer many promising advantages to be applied in the medical fields for preparation of new advanced dosage forms: high drug-loading capacity which lowers the possibilities of chemical interactions or toxicity, high surface area-to-volume ratio, ease of manipulation for parenteral administration due to particle size and surface characteristics of nanoparticles, capability to use for active and passive drug-targeting strategies, sustained and controlled release purposes of drug production, and site-specific targeting by magnetic guidance or by attaching targeting ligands to the surface of particles [17]. There are many factors which affect the method of selection for the nanoparticle manufacturing materials such as required nanoparticle size, targeting properties, lipid or water solubility and their respected hydrophobicity or hydrophilicity, chemical and physical stability, surface charge and permeability, biodegradability, biocompatibility, cytotoxicity, drug release profile, and antigenicity of the final product [18].

Blood-brain barriers challenge the drug delivery design. In general, pharmaceutical drug dosage forms cannot easily cross the BBB; however, they can pass only by active efflux or carrier-mediated transport in the usual drug formulations with very little bioavailability [19, 20]. In vivo and in vitro studies verified the passage of nanoparticles through the BBB. They supported the incorporation of the nanotherapeutic substances into the brain, so nanoparticles can also be applied in diagnosis as well as brain-targeted therapy and gene therapy [21–23].

Ideal nanoparticles properties for brain drug delivery purposes:

(1) Nanoparticles must be nontoxic, biodegradable, and biocompatible, e.g., polylactide homopolymers and polylactide-co-glycolide polymer nanoparticles [24].

(2) Nanoparticle size is preferred to be lower than 100 nm where the rate of clearance increases with increasing particle size more than 100 nm, so it affects both the biodistribution and bioavailability [25].

(3) Physical stability and preventing aggregation in the blood is necessary, where several types of nanoparticles were considered to be toxic due to physical rather than chemical surface properties [26].

(4) Prolonged blood circulation time, in which only PEGylated nanoparticles had lower uptake and prolonged time [27].

(5) Targeted brain delivery with no need for active reflux or carrier-mediated pathway, so as to enhance drug bioavailability and efficacy and reduce the required therapeutic dose and its resultant efficacy.

(6) Noninvasive gene-targeting brain delivery, e.g., PEGylated immunoliposomes via receptor-mediated transcytosis which enter their content into the brain tissues without injuring the BBB [28].

(7) Cost-effective studies should evaluate the potential usage of nanomedicine for clinical purposes.

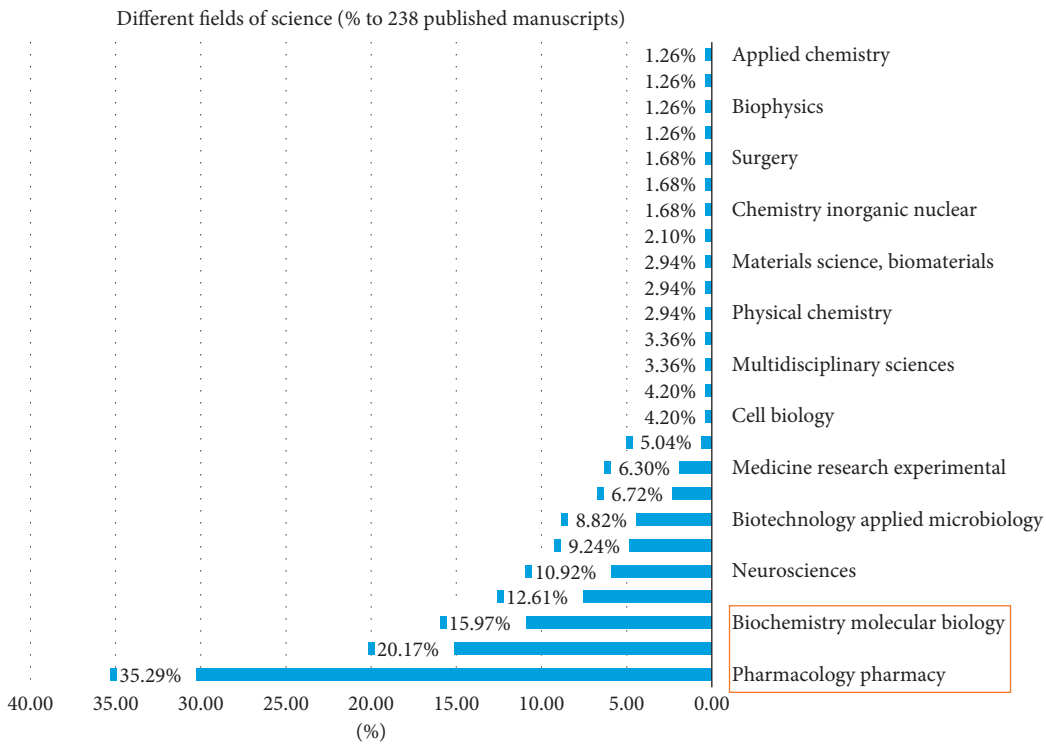

Figure 1: Different fields of science interested in using nanotechnology for the management of NDDs.

Increasing treatment cost will limit the number of patients who can benefit from those medications [29].

3. Experimental Applications of Nanoparticles in Treatment of Neurodegenerative Diseases

3.1. Therapeutic Challenges. Recent application of nanotechnology in biomedicine and the optimistic growing of researchers and applications in the fields of nanomedicine and neuroscience provide the scientists with a promising hope for the investigation and management of NDDs. The applications include targeted drug delivery, diagnostic services, and manufacturing of advanced biocompatible substances [30, 31]. Solid nanoparticles are novel potential colloidal carrier systems and matrix-like units prepared by polymers or lipids; they are administered parenterally by the intravenous route. This technology manipulates nanometer-scaled (1–100 nm) bioengineered materials with functional groups that can interact at the molecular level with biological systems [32]. Understanding these bioengineered nanoparticles is a vital key to recognize various nanomedical applications. The unique features of nanoparticles lie behind their attractiveness for medical purposes. The features are a very high surface area of the nanoparticles to the mass ratio and the ability to be functioning at their surface, so they can adsorb or carry other substances such as medicines, diagnostic, or therapeutic probes and proteins. Nanoparticles can be prepared with specific quantum properties which are promising in diagnostic and imaging purposes [33].

Figure 2 illustrates different types of nanoparticles with their average nanosize that can be injected intracerebrally to treat Alzheimer disease.

4. Recent Applications of Nanoparticles in the Management of Neurodegenerative Diseases (NDDs)

Peptide-polymer conjugates profoundly improved bioavailability and brain delivery of drugs. They advance pharmacokinetics by raising their molecular mass, so they shield themselves from proteolytic enzymes. These novel approaches created new opportunities for the future development of neurotherapeutic drugs and offer great hope for the treatment of brain diseases [34, 35]. Despite the clinical potentiality of the peptides, native peptides have been seen with limited pharmacokinetics. They have low bioavailability and metabolic stability in normal physiological conditions [36]. Several interventions aimed to enhance biological features of peptides for clinical applications by inclusion of synthetic amino acids, pseudopeptide bonding, cyclization, and chemical modification by conjugation to polymers such as in different nanoparticle systems offer great hope in the treatment of brain dysfunctions [37].

THPdb (http://crdd.osdd.net/raghava/thpdb/) a database of the Food and Drug Administration (FDA) contains therapeutically approved peptides and proteins in which the data from 985 manuscripts and 70 patents were compiled. The latest version of the THPdb database includes full information on 239 US FDA-approved

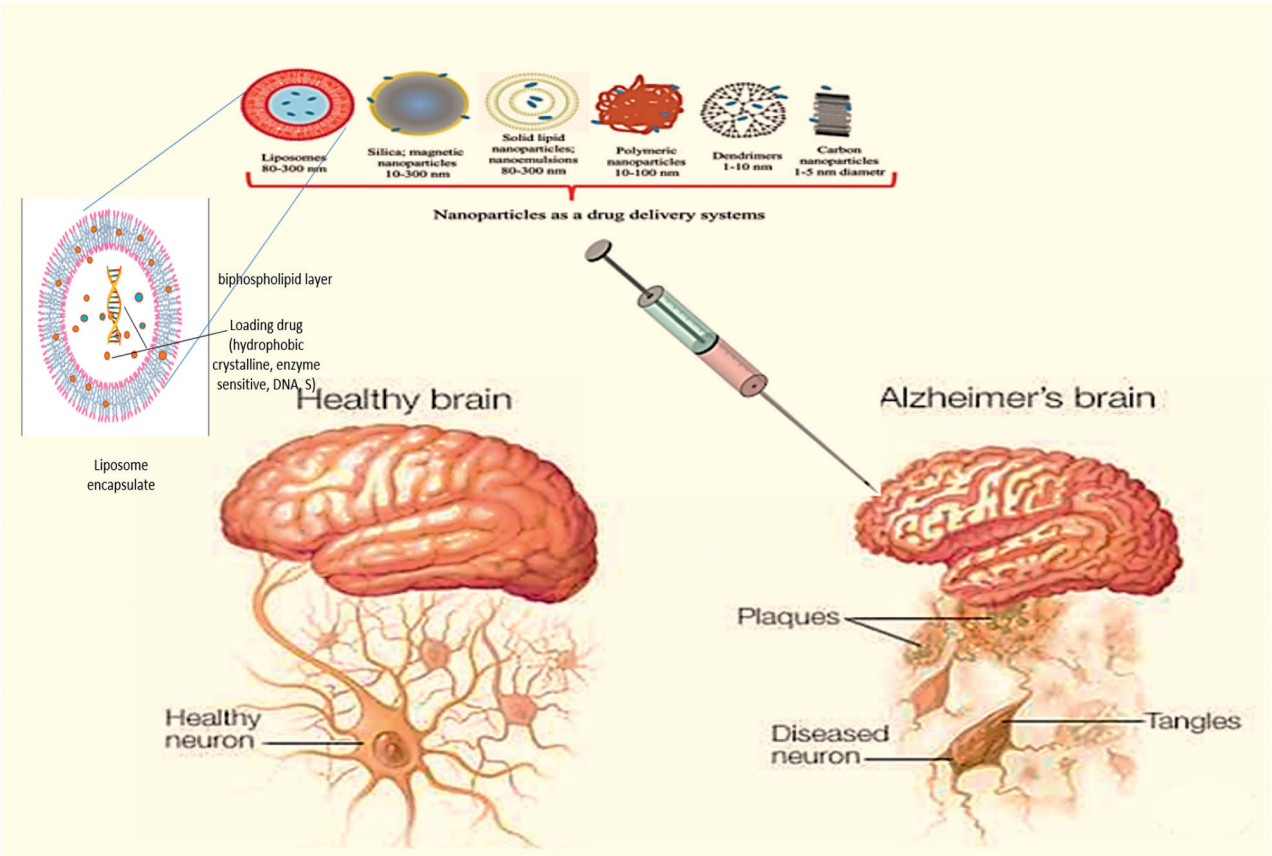

Figure 2: Diagrammatic ICV injection for different forms of drug-loaded nanosystems.

therapeutic peptides and proteins and their 380 drug derivatives [38]. The latest nanocarrier system was designed by Yemisci et al., where chitosan nanoparticles were used as a carrier for small peptides such as caspase inhibitor Z-DEVD-FMK or the large peptide-like fibroblast growth factor through the BBB. These nanoparticles are selectively targeting the brain without passing the liver and spleen [39]. The route of nanoparticle administration reveals essential attention to defeat the physiological BBB and to achieve therapeutic drug concentrations therein. Therefore, alternative routes of administration for brain drug delivery are being developed, such as the intravenous and oral route, inhalation or intratracheal, and intrathecal drug delivery systems [40]. There is a growing interest in developing targeted brain delivery medicines and polymeric or lipid nanoparticles, which have a high degree of specificity, to neurorepair and protection. The main aim in the design of a drug delivery nanosystem is to protect therapeutic agents and increase their biodistribution and therapeutic index to the brain [41]. These nanosystems such as nanoparticles including nanospheres and nanocapsules, micelles, dendrimers, nanocrystals, and nanogolds mainly contain polymer- or lipid-based carriers. Nanoparticles represent a promising strategy in which the polymeric and biocompatible devices could deliver immunoprotected therapeutic compounds to the brain [42].

5. Advances of Nanoparticles in the Management of Alzheimer Disease (AD)

Alzheimer's disease (AD) is a progressive neurodegenerative disease that is manifested by deterioration of cognitive, neuropsychiatric, and behavioral motor functions. Accumulation of beta amyloid aggregates is the hallmark of AD which are neurotoxic, and the resultant oxidative stress causes damage to neurons and brain cells. The main aim of AD therapy is to protect neurons against the oxidative stress, antiamyloid therapy, degeneration, and to pass through the BBB for brain-targeted action [43]. In vitro and in vivo studies for managing AD were done by Liu et al. in 2016 using a mice model; they successfully achieved therapeutic brain delivery by parenteral injection of a multifunctional nanoparticle. This multifunctional nanosystem used PEGylated dendrigraft poly-l-lysine as a carrier of the therapeutic gene and the peptide [44]. Cranial implants of microencapsulated vascular endothelial growth factor-(VEGF-) secreting cells elevated brain vessel formation in the cerebral cortex corresponding to the control group. Findings of this study proved the earlier fact that considers VEGF has a potential therapeutic effect on brain disorders such as angiogenesis, protection of neurons, and cerebral microvascular exchange of nutrients [45, 46]. Direct injection of bolus doses of drug nanoparticles into the brain has many advantages: high concentration in the brain was

Table 1: Drugs used for investigating the effective therapy of different nanoparticles in the treatment of Alzheimer.

Drug	Composite	Type of nanoparticles	Model	Improved properties	Shape and particle size	Zeta potential	References
Pd hydride (PdH)	Pd hydride (PdH)	Nanoparticles	Mice	In situ and sustained release of high payload of hydrogen, decreasing the oxidative stress	Cubic shape with uniform size (about 30 nm)	NA	[61]
Vitamin D-binding protein (DBP)	DBP-PLGA	Nanoparticles	Aβ-overexpressing (5XFAD) mice	Decrease Aβ aggregation and accumulation	Spherical and uniform size, average 226.6 ± 44.4 nm	−0.144 mV	[62]
Curcumin (Cu) and selenium (Se)	Se-Cur/PLGA	Nanospheres	Transgenic mice (5XFAD)	Decreases the amyloid-β	Spherical and uniform size, average 70.5 ± 6 nm	NA	[63]
SNPs	Aqueous extraction of *Lampranthus coccineus*, *Malephora lutea*, F. Aizoaceae	Nanoparticles	Adult male albino rats of Sprague Dawley	Anticholinesterase and antioxidant activity	Spherical nanoparticles with a mean size from 12.86 nm to 28.19 nm	NA	[64]
Aβ1-42 peptide	A$\beta_{1\text{-}42}$ peptide monoclonal antibody to PEG chain (anti-aβ1-42-NPs)	PEGylated nanoparticles	AD-like transgenic mice	Promote A$\beta_{1\text{-}42}$ elimination through the "*sink effect*"	125 nm	−20 to −30 mV	[65]
Zinc	Zinc-PLGA	Nanoparticles	Wild-type (WT) and APP23 mice	Reduction in plaque size and affects the release of proinflammatory cytokines IL-6 and IL-18	200–220 nm	NA	[66]
Coumarin	TQNP/H102	Nanoparticles	APP/PS1 transgenic mice	Decreasing amyloid plaques, increasing *Aβ*-degrading enzymes, reducing tau protein phosphorylation, protecting synapses, and improving the spatial learning and memory	100 nm that may increase on loading with H102 peptide	−25 mV	[67]

DBP-PLGA: vitamin D-binding protein loaded PLGA (poly (D,L-lactic acid-co-glycolic acid)); Se: selenium; Aβ: amyloid beta protein; TQNP is a multifunctionalized nanoparticle system based on poly(ethylene glycol)-poly(lactic acid) (PEG-PLA) and modified with TGN peptides as the brain ligand and QSH peptides for A42-binding (TQNP) [61], to target amyloid plaques in the brain; TGN (TGNYKALHPHNGC), QSH (QSHYRHISPAQVC), H102 peptide (HKQLPFFEED), and Aβ42 were peptides; NA: not available; SNPs: silver nanoparticles.

achieved with no alteration or impairment in BBB functions, enhancement of vascularity at the cerebral cortex, and diminishing of the amyloid beta deposits [47]. Based on this fact, the therapeutic use of VEGF microencapsulation was patented [48, 49]. Parenteral administration of medications ensures the delivering of therapeutic medicines with proper doses to the cerebrospinal compartments, but it exposes the ependymal surface to a higher level of drugs that may cause toxic rather than therapeutic effects. Treatment with growth factor nanoreleasing systems is highly promising for NDDs, but it may cause severe side effects in the brain due to the direct injection to the brain. Axonal sprouting and Schwann cell hyperplasia were reported after the intracerebroventricular (ICV) injection of the nerve growth factor [50]. Periventricular astrogliosis is also reported due to the ICV injection of the fibroblast growth factor [51].

Another design of physiologically active nanoparticles is the cytokine-derived peptide nanopeptide that is used in the preparation of drug dosage forms for the management of NDDs, in precise, AD [52]. They can be administered by parenteral, topical, oral prelingual, rectal, or intraocular routes, but the preferred routes are subcutaneous, intranasal, intraperitoneal (IV), and intravenous routes (IP). Topical preparations such as patch, pomade, or gel are available [53]. Experimental studies proved that the PAT nanopeptide exhibits some biological activity when it is administered by the ICV route—which bypasses the BBB—and by the parenteral route (intraperitoneal). This latter mode of administration highlights the fact that that the product crosses the BBB and reaches the brain. To pass the BBB, persons skilled in the art know that the molecular and physicochemical properties of the molecule must fulfil the rule-of-five criteria described by Lipinski et al. (a low molecular weight, its

lipophilicity, its charge, etc.). However, it was a surprise to notice that the PAT peptide, which does not fulfil all these criteria, crosses the BBB [54].

Monoclonal antibodies have been anticipated as useful options for both in vivo diagnosis and treatment. Recent clinical trials have assumed that this promising potential impact is becoming a reality. Attention of researchers is moving towards the production of sufficient quantity of monoclonal antibodies with high purity and quality for widespread human use. Microencapsulation technique is currently used for large-scale production of both human and murine types of monoclonal antibodies for in vivo applications [55]. Encapsulated antibodies are now used for the treatment of brain diseases. Microencapsulation used for controlled drug delivery of anti-VE-cadherin monoclonal antibodies can be considered as a new therapeutic option for the inhibition of angiogenesis [56]. Nanoparticle encapsulation of the drug maintains about 80% of its enzymatic activity with no cytotoxicity at the level of therapeutic concentration [57].

A novel product of siRNA nanoparticles used the peptide-tagged polyethylene glycol- (PEG-) related chitosan polymer as a drug delivery system for NDD applications. It is used to deliver a functional siRNA against the *Ataxin-1* gene in an in vitro simulation of NDD. The results indicate that the SCA1 protein was successfully suppressed after 48 hr of transfection. The result of this study has great impact on NDD like AD, PD, and others [58]. Cerium oxide nanoparticles (CeONPs) have recently appeared as a new therapeutic option which extends the therapeutic impact of using nanomedicine in the treatment of NDD such as the AD, PD, multiple sclerosis, ischemic stroke, and amyotrophic lateral sclerosis. Their average nanosize helps the smooth passage through the BBB. However, its antioxidant activity can change the signaling pathway, which enables the scavenging of reactive oxygen radicals [59]. Novel galantamine-loaded polymeric nanoparticles are another recently emerged drug delivery systemþþ for treating neurodegenerative diseases. Galantamine-loaded polymeric nanoparticles (GNPs) were prepared by the nanoemulsion templating technique, and GNPs have safe, biocompatible, and biodegradable properties which make them suitable for the intravenous use [57]. Silica nanoparticles (SiNPs) are widely used as a drug delivery carrier and also used in molecular detection and cellular manipulations, and many research studies try to apply them in the nanoneuro-medical applications. However, SiNPs may dangerously affect the brain by causing neurotoxicity, inflammation, and degeneration by its amyloidogenesis action, which is a hallmark of Alzheimer's disease [60].

Table 1 summarizes some recent pharmacological studies that investigate the effective therapy of different nanoparticles in the treatment of Alzheimer.

6. Conclusion

Targeted nanoparticle brain drug delivery aims to improve the clinical outcomes with developing the diagnostics and therapeutic efficacy of medication in managing Alzheimer disease. Many efforts on this approach were done and are still ongoing for effective symptomatic therapy, suspending the progression of different types of neurodegenerative diseases and decreasing the well-known severe complications of therapeutic medication. Some nanopharmaceuticals are patented in treating NDDs in animals, some still in the experimental stage, and some proved to be safe, while others reported cytotoxicity. Identification of putative gene-targeted therapy using compacted DNA and RNA plasmids using viral or nonviral vector technique research studies are also still going on, and all these studies are promising for managing and may preventing NDDs, but until now there is no evidence for the efficacy and safety margin of using nanoparticles in patients with AD.

Conflicts of Interest

The authors of this paper have no conflicts of interest that influence the results or interpretation of reviewed manuscripts.

References

[1] B. L. Rajak, M. Gupta, and D. Bhatia, "Growth and advancements in neural control of limb," *Biomedical Science and Engineering*, vol. 3, no. 3, pp. 46–64, 2015.

[2] S. S. Dikmen, J. E. Machamer, J. M. Powell, and N. R. Temkin, "Outcome 3 to 5 years after moderate to severe traumatic brain injury11No commercial party having a direct financial interest in the results of the research supporting this article has or will confer a benefit upon the author(s) or upon any organization with which the author(s) is/are associated," *Archives of Physical Medicine and Rehabilitation*, vol. 84, no. 10, pp. 1449–1457, 2003.

[3] Y. Choonara, V. Pillay, L. Du Toit et al., "Trends in the molecular pathogenesis and clinical therapeutics of common neurodegenerative disorders," *International Journal of Molecular Sciences*, vol. 10, no. 6, pp. 2510–2557, 2009.

[4] L. Bertram and R. E. Tanzi, "The genetic epidemiology of neurodegenerative disease," *Journal of Clinical Investigation*, vol. 115, no. 6, pp. 1449–1457, 2005.

[5] A. W. J. Morris, M. M. Sharp, N. J. Albargothy et al., "Vascular basement membranes as pathways for the passage of fluid into and out of the brain," *Acta Neuropathologica*, vol. 131, no. 5, pp. 725–736, 2016.

[6] P. Dayalu and R. L. Albin, "Huntington disease," *Neurologic Clinics*, vol. 33, no. 1, pp. 101–114, 2015.

[7] Web of Science, "Nanotechnology neurodegenerative diseases," *Results Analysis*, 2020, https://wcs-webofknowledge-com.sdl.idm.oclc.org/RA/analyze.do?product=WOS&SID=E39jrRpJaOJawVLdYQc&field=TASCA_JCRCategories_JCRCategories_en&yearSort=false.

[8] C. Saraiva, C. Praça, R. Ferreira, T. Santos, L. Ferreira, and L. Bernardino, "Nanoparticle-mediated brain drug delivery: overcoming blood-brain barrier to treat neurodegenerative diseases," *Journal of Controlled Release*, vol. 235, pp. 34–47, 2016.

[9] Z. Izadi, A. Divsalar, A. A. Saboury, and L. Sawyer, "β-lactoglobulin-pectin nanoparticle-based oral drug delivery system for potential treatment of colon cancer," *Chemical Biology & Drug Design*, vol. 88, no. 2, pp. 209–216, 2016.

[10] L. Casettari and L. Illum, "Chitosan in nasal delivery systems for therapeutic drugs," *Journal of Controlled Release*, vol. 190, pp. 189–200, 2014.
[11] J. Kreuter, "Drug delivery to the central nervous system by polymeric nanoparticles: what do we know?" *Advanced Drug Delivery Reviews*, vol. 71, pp. 2–14, 2014.
[12] K. Nakano, J.-I. Koga, and K. Egashira, "Nanoparticle-mediated endothelial cell-selective drug delivery system," in *Therapeutic Angiogenesis*, pp. 247–266, Springer, Berlin, Germany, 2017.
[13] J. Zhou, T. R. Patel, J. M. Piepmeier, and W. M. Saltzman, "Highly penetrative nanocarriers for treatment of CNS disease," US 20150118311A1, 2020.
[14] A. Vashist, A. Kaushik, A. Vashist et al., "Nanogels as potential drug nanocarriers for CNS drug delivery," *Drug Discovery Today*, vol. 23, no. 7, pp. 1436–1443, 2018.
[15] N. Rajput, "Methods of preparation of nanoparticles-a review," *International Journal of Advances in Engineering & Technology*, vol. 7, no. 6, p. 1806, 2015.
[16] G. Modi, V. Pillay, and Y. E. Choonara, "Advances in the treatment of neurodegenerative disorders employing nanotechnology," *Annals of the New York Academy of Sciences*, vol. 1184, no. 1, pp. 154–172, 2010.
[17] G. Tiwari, R. Tiwari, S. Bannerjee et al., "Drug delivery systems: an updated review," *International Journal of Pharmaceutical Investigation*, vol. 2, no. 1, p. 2, 2012.
[18] K. G. Budinski and M. K. Budinski, *Engineering Materials*, Pearson Education India, Bengaluru, India, 1949.
[19] L. Battaglia, P. P. Panciani, E. Muntoni et al., "Lipid nanoparticles for intranasal administration: application to nose-to-brain delivery," *Expert Opinion on Drug Delivery*, vol. 15, no. 4, pp. 369–378, 2018.
[20] C. A. Peptu, L. Ochiuz, L. Alupei, C. Peptu, and M. Popa, "Carbohydrate based nanoparticles for drug delivery across biological barriers," *Journal of Biomedical Nanotechnology*, vol. 10, no. 9, pp. 2107–2148, 2014.
[21] T.-T. Zhang, W. Li, G. Meng, P. Wang, and W. Liao, "Strategies for transporting nanoparticles across the blood-brain barrier," *Biomaterials Science*, vol. 4, no. 2, pp. 219–229, 2016.
[22] R. Bayford, T. Rademacher, I. Roitt, and S. X. Wang, "Emerging applications of nanotechnology for diagnosis and therapy of disease: a review," *Physiological Measurement*, vol. 38, no. 8, pp. R183–R203, 2017.
[23] O. Betzer, M. Shilo, R. Opochinsky et al., "The effect of nanoparticle size on the ability to cross the blood-brain barrier: an in vivo study," *Nanomedicine*, vol. 12, no. 13, pp. 1533–1546, 2017.
[24] F. Masood, "Polymeric nanoparticles for targeted drug delivery system for cancer therapy," *Materials Science and Engineering: C*, vol. 60, pp. 569–578, 2016.
[25] N. Hoshyar, S. Gray, H. Han, and G. Bao, "The effect of nanoparticle size on in vivo pharmacokinetics and cellular interaction," *Nanomedicine*, vol. 11, no. 6, pp. 673–692, 2016.
[26] A. Gnach, T. Lipinski, A. Bednarkiewicz, J. Rybka, and J. A. Capobianco, "Upconverting nanoparticles: assessing the toxicity," *Chemical Society Reviews*, vol. 44, no. 6, pp. 1561–1584, 2015.
[27] H. Ou, T. Cheng, Y. Zhang et al., "Surface-adaptive zwitterionic nanoparticles for prolonged blood circulation time and enhanced cellular uptake in tumor cells," *Acta Biomaterialia*, vol. 65, pp. 339–348, 2018.
[28] A. V. Kabanov and E. V. Batrakova, "Polymer nanomaterials for drug delivery across the blood brain barrier," in *Neuroimmune Pharmacology*, pp. 847–868, Springer, Berlin, Germany, 2017.
[29] D. M. Parikh, *Handbook of Pharmaceutical Granulation Technology*, CRC Press, Boca Raton, FL, USA, 2016.
[30] S. B. Pehlivan, "Nanotechnology-based drug delivery systems for targeting, imaging and diagnosis of neurodegenerative diseases," *Pharmaceutical Research*, vol. 30, no. 10, pp. 2499–2511, 2013.
[31] O. Lupan, "Nanotechnology and its applications in medicine," in *Health Technology Management*, Institutional Repository of the Technical University of Moldova (IRTUM), Chişinău, Moldova, 2016.
[32] V. J. Pansare, *Fundamental and Applied Studies in Nanoparticle Biomedical Imaging, Stabilization, and Processing*, Princeton University, Princeton, NJ, USA, 2015.
[33] L. A. Lane, X. Qian, and S. Nie, "SERS nanoparticles in medicine: from label-free detection to spectroscopic tagging," *Chemical Reviews*, vol. 115, no. 19, pp. 10489–10529, 2015.
[34] J. Ren, R. Zhang, and J. M. Regenstein, "Adding biological function to nonbiological nanoparticles," in *Nutrient Delivery*, pp. 497–534, Elsevier, Amsterdam, Netherlands, 2017.
[35] W. Chen, C. Zhan, B. Gu et al., "Targeted brain delivery of itraconazole via RVG29 anchored nanoparticles," *Journal of Drug Targeting*, vol. 19, no. 3, pp. 228–234, 2011.
[36] F. Antunes, F. Andrade, D. Ferreira, H. Morck Nielsen, and B. Sarmento, "Models to predict intestinal absorption of therapeutic peptides and proteins," *Current Drug Metabolism*, vol. 14, no. 1, pp. 4–20, 2013.
[37] L. Gentilucci, R. De Marco, and L. Cerisoli, "Chemical modifications designed to improve peptide stability: incorporation of non-natural amino acids, pseudo-peptide bonds, and cyclization," *Current Pharmaceutical Design*, vol. 16, no. 28, pp. 3185–3203, 2010.
[38] S. S. Usmani, G. Bedi, J. S. Samuel et al., "THPdb: database of FDA-approved peptide and protein therapeutics," *PloS One*, vol. 12, no. 7, 2017.
[39] M. Yemisci, S. Caban, Y. Gursoy-Ozdemir et al., "Systemically administered brain-targeted nanoparticles transport peptides across the blood-brain barrier and provide neuroprotection," *Journal of Cerebral Blood Flow & Metabolism*, vol. 35, no. 3, pp. 469–475, 2015.
[40] C. V. Pardeshi and V. S. Belgamwar, "Direct nose to brain drug deliveryviaintegrated nerve pathways bypassing the blood-brain barrier: an excellent platform for brain targeting," *Expert Opinion on Drug Delivery*, vol. 10, no. 7, pp. 957–972, 2013.
[41] G. Tosi, B. Bortot, B. Ruozi et al., "Potential use of polymeric nanoparticles for drug delivery across the blood-brain barrier," *Current Medicinal Chemistry*, vol. 20, no. 17, pp. 2212–2225, 2013.
[42] S. C. Tang, *Impact of Apical ABC Transporters on Pharmacokinetics of Targeted Anticancer Drugs*, Utrecht University, Utrecht, Netherlands, 2013.
[43] A. Nazem and G. A. Mansoori, "Nanotechnology solutions for Alzheimer's disease: advances in research tools, diagnostic methods and therapeutic agents," *Journal of Alzheimer's Disease*, vol. 13, no. 2, pp. 199–223, 2008.
[44] Y. Liu, S. An, J. Li et al., "Brain-targeted co-delivery of therapeutic gene and peptide by multifunctional nanoparticles in Alzheimer's disease mice," *Biomaterials*, vol. 80, pp. 33–45, 2016.
[45] A. Larpthaveesarp, D. Ferriero, and F. Gonzalez, "Growth factors for the treatment of ischemic brain injury (growth

factor treatment)," *Brain Sciences*, vol. 5, no. 2, pp. 165–177, 2015.

[46] E. Herrán, R. Pérez-González, M. Igartua, J. L. Pedraz, E. Carro, and R. M. Hernández, "VEGF-releasing biodegradable nanospheres administered by craniotomy: a novel therapeutic approach in the APP/Ps1 mouse model of Alzheimer's disease," *Journal of Controlled Release*, vol. 170, no. 1, pp. 111–119, 2013.

[47] G. Orive, R. M. Hernández, A. R. Gascón et al., "Cell encapsulation: promise and progress," *Nature Medicine*, vol. 9, no. 1, pp. 104–107, 2003.

[48] N. J. Abbott, "Blood-brain barrier structure and function and the challenges for CNS drug delivery," *Journal of Inherited Metabolic Disease*, vol. 36, no. 3, pp. 437–449, 2013.

[49] X. Tian, O. Brookes, and G. Battaglia, "Pericytes from mesenchymal stem cells as a model for the blood-brain barrier," *Scientific Reports*, vol. 7, no. 1, pp. 1–7, 2017.

[50] J. C. M. Schlachetzki, D. P. Pizzo, D. A. Morrissette, and J. Winkler, "Intracerebroventricular administration of nerve growth factor induces gliogenesis in sensory ganglia, dorsal root, and within the dorsal root entry zone," *BioMed Research International*, vol. 2014, Article ID 704259, 9 pages, 2014.

[51] P. D. Le Roux and S. Esquenazi, "Astrocytes mediate cerebral cortical neuronal axon and dendrite growth, in part, by release of fibroblast growth factor," *Neurological Research*, vol. 24, no. 1, pp. 81–92, 2002.

[52] H. Temsamani, S. Krisa, J.-M. Mérillon, and T. Richard, "Promising neuroprotective effects of oligostilbenes," *Nutrition and Aging*, vol. 3, no. 1, pp. 49–54, 2015.

[53] D. O'neil, "Peptides and their use," US 9169290B2, 2015.

[54] C. A. Lipinski et al., "Experimental and computational approaches to estimate solubility and permeability in drug discovery and development settings," *Advanced Drug Delivery Reviews*, vol. 23, no. 1-3, pp. 3–25, 1997.

[55] R. G. Duff, "Microencapsulation technology: a novel method for monoclonal antibody production," *Trends in Biotechnology*, vol. 3, no. 7, pp. 167–170, 1985.

[56] C. Spuch and C. Navarro, "Cell microencapsulation implants into the central nervous system," *Recent Patents on Nanomedicinee*, vol. 1, no. 1, pp. 60–67, 2011.

[57] M. M. Wen, N. S. El-Salamouni, W. M. El-Refaie et al., "Nanotechnology-based drug delivery systems for Alzheimer's disease management: technical, industrial, and clinical challenges," *Journal of Controlled Release*, vol. 245, pp. 95–107, 2017.

[58] M. Malhotra, C. Tomaro-Duchesneau, and S. Prakash, "Synthesis of TAT peptide-tagged PEGylated chitosan nanoparticles for siRNA delivery targeting neurodegenerative diseases," *Biomaterials*, vol. 34, no. 4, pp. 1270–1280, 2013.

[59] S. Naz, J. Beach, B. Heckert et al., "Cerium oxide nanoparticles: a "radical" approach to neurodegenerative disease treatment," *Nanomedicine*, vol. 12, no. 5, pp. 545–553, 2017.

[60] Y. Li, J. Fan, and D. Ju, "Neurotoxicity concern about the brain targeting delivery systems," in *Brain Targeted Drug Delivery System*, pp. 377–408, Elsevier, Amsterdam, Netherlands, 2019.

[61] L. Zhang, P. Zhao, C. Yue et al., "Sustained release of bioactive hydrogen by Pd hydride nanoparticles overcomes Alzheimer's disease," *Biomaterials*, vol. 197, pp. 393–404, 2019.

[62] S. G. Jeon, M.-Y. Cha, J.-I. Kim et al., "Vitamin D-binding protein-loaded PLGA nanoparticles suppress Alzheimer's disease-related pathology in 5XFAD mice," *Nanomedicine: Nanotechnology, Biology and Medicine*, vol. 17, pp. 297–307, 2019.

[63] X. Huo, Y. Zhang, X. Jin, Y. Li, and L. Zhang, "A novel synthesis of selenium nanoparticles encapsulated PLGA nanospheres with curcumin molecules for the inhibition of amyloid β aggregation in Alzheimer's disease," *Journal of Photochemistry and Photobiology B: Biology*, vol. 190, pp. 98–102, 2019.

[64] K. A. Youssif, E. G. Haggag, A. M. Elshamy et al., "Anti-Alzheimer potential, metabolomic profiling and molecular docking of green synthesized silver nanoparticles of Lampranthus coccineus and Malephora lutea aqueous extracts," *PloS One*, vol. 14, no. 11, 2019.

[65] D. Carradori, C. Balducci, F. Re et al., "Antibody-functionalized polymer nanoparticle leading to memory recovery in Alzheimer's disease-like transgenic mouse model," *Nanomedicine: Nanotechnology, Biology and Medicine*, vol. 14, no. 2, pp. 609–618, 2018.

[66] A. Vilella, D. Belletti, A. K. Sauer et al., "Reduced plaque size and inflammation in the APP23 mouse model for Alzheimer's disease after chronic application of polymeric nanoparticles for CNS targeted zinc delivery," *Journal of Trace Elements in Medicine and Biology*, vol. 49, pp. 210–221, 2018.

[67] X. Zheng, C. Zhang, Q. Guo et al., "Dual-functional nanoparticles for precise drug delivery to Alzheimer's disease lesions: targeting mechanisms, pharmacodynamics and safety," *International Journal of Pharmaceutics*, vol. 525, no. 1, pp. 237–248, 2017.

Hindawi
Journal of Nanotechnology
Volume 2020, Article ID 3139701, 9 pages
https://doi.org/10.1155/2020/3139701

Research Article

Synthesis of Specific ZnF Based Nanoparticles ($ZnFe_2O_4$): Antimicrobial Properties, Surface Characteristics, and Adsorption Activity for AB 29 Textile Dye

Ferda Gönen and Gökhan Tekinerdoğan

Mersin University, Chemical Engineering Department, Mersin 33343, Turkey

Correspondence should be addressed to Ferda Gönen; gonenf74@gmail.com

Received 16 September 2019; Accepted 14 February 2020; Published 2 July 2020

Guest Editor: Giorgio Vilardi

In this investigation, the color removal from synthetic wastewaters containing Acid Blue 29 (AB 29) dye was investigated by ZnF-based nanomaterials ($ZnFe_2O_4$) synthesized by the coprecipitation method in a batch system. SEM, FT–IR, and XRD analysis were used for the characterization of the nanoparticles (before and after adsorption), and the analysis results were compared with each other. The parameters such as pH, temperature, dye concentration, and nanoparticle dosage affecting color removal were examined systematically, and favorable color removal conditions were determined by the classical approach. From the experimental results, the favorable conditions with high removal efficiency for the adsorption were determined: removal temperature 35°C and the removal pH 2.0. At these experimental conditions, the adsorbed dye amount per unit mass of adsorbent and the percentage dye removal were determined as 1489.79 $mg{\cdot}g^{-1}$ and 98.83%, respectively. In the other part of the research, three different isotherm models (Langmuir, Freundlich, and Temkin) were used to examine the adsorption equilibrium data. Langmuir and especially Freundlich linear isotherm models provided the highest R^2 regression coefficients, successfully. The kinetic data was evaluated by pseudo-first-order and pseudo-second-order kinetic model approach. It was observed that pseudo-second-order kinetic model best represented AB 29-ZnF adsorption kinetic data. The determined thermodynamic parameters such as ΔH, ΔS, and ΔG were proved that the AB 29-ZnF adsorption system was an exothermic ($\Delta H < 0$), spontaneous, thermodynamically favorable ($\Delta G < 0$), and stabilized system without any structural changes in sorbate and sorbents ($\Delta S<0$).

1. Introduction

The color caused by domestic and industrial pollution sources is undesirable for the aesthetic appearance of water [1, 2]. Also the discharge of textile industry wastewaters including large amount of azo dyes having nonbiodegradability, toxicity, and carcinogenic properties poses a major threat to the ecosystem and especially aquatic life depending on their high concentration and stability in wastewaters [3, 4]. Reactive dyestuffs are an important class of commercially important textile dyestuffs. On the other hand, these reactive dyestuffs are one of the most stable and polluting dyestuffs during the dyeing process. Reactive dyes exhausted are about 50% in their hydrolysed and unfixed form during the washing process, and treatment of them is problematic [5–7].

Physical, chemical, and biological treatment methods are presently used for textile wastewater treatment. These methods are osmosis, chlorination, ozonation, filtration, oxidation processes, nanofiltration, chemical precipitation, ion exchange, and chemical coagulation/flocculation. The conventional biological treatment methods may not provide adequate treatment for the complete color removal and degradation of organics and dyes. Physical/physicochemical methods such as coagulation and ion exchange are not frequently preferred for wastewater treatment because of high operational costs. Chlorination and ozonation processes cause degradation by chemical reaction and allow breaking down harmful large into smaller ones. Moreover, discharching chlorinated compounds to the environment causes some serious environmental problems. Also,

ozonation is an unstable process and requires large capital expenses depending on the need for immediate use for rapid chemical process. Many researchers have investigated water treatment containing color removal by adsorption using low cost and environmentally compatible materials [8–10]. When investigations conducted in recent years are examined, there is a limited number of investigations using magnetic, antimicrobial, and suitable for more than one application especially for color removal from wastewaters containing chemical and biological pollution load. In this investigation, the synthetically prepared wastewater solutions containing AB 29 dye were examined for the color removal by ZnF-based nanoparticle. The novelty of this research is the use of ZnF-based nanomaterial with superior advantages such as low cost, antimicrobial, and environmentalist characteristics in treatment of textile dye solution. The most important advantages of ZnF-based nanomaterials is antimicrobial property to many harmful pathogens. So, this investigation proved the removal of two different types of pollutant load (biological and chemical) in domestic and/or industrial wastewater with high efficiency by using only one novel adsorbent, $ZnFe_2O_4$.

2. Experiments

2.1. Reagents. In order to synthesize the zinc oxide ($ZnFe_2O_4$) nanoparticles, Iron (III) chloride ($FeCl_3$), zinc chloride ($ZnCl_2$), sodium hydroxide (NaOH), and hydrochloric acid (HCl) reagents were obtained from Merck. Moreover, AB 29 dye was obtained from Sigma-Aldrich.

Bacillus subtilis, *Klebsiella pneumoniae*, *Escherichia coli*, and *Enterococcus fecalis* bacteria obtained from Mersin University Microbiology Laboratory of the Biology Department were used during the investigation of antimicrobial effect of ZnF-based adsorbent.

2.2. Synthesis of Nanoparticles. ZnF-based nanomaterials were synthesized by the coprecipitation method for the adsorption of AB 29 dye solution. 200 mL of 0.75 M Iron (III) chloride ($FeCl_3$) and 200 mL of 0.25 M zinc chloride ($ZnCl_2$) solutions were mixed with each other, and then the solution was stirred. After that, 2 M NaOH solution was added to this mixture while the pH value was 10 in a magnetic stirrer at 60°C. The final solution was filtered at 60°C for 18 hours. The drained solution was calcined in an ash oven at 300°C, and the synthesized particles were converted into powdered particles in the mortar [11].

2.3. Characterization Experiments. FTIR (Perkin Elmer, Fourier Transform Infrared Spectrometer), SEM (ZeissSupra 55 Area Emission, Scanned Electron Microscope), and XRD (Philips, X'Pert brand X-ray Diffractometer) were used for identification of morphological properties and identification of phases and crystal structures of synthesized particles at Mersin University Advanced Materials Research Center (MEITAM).

2.4. Color Removal Experiments. Color removal experiments were carried out at 120 rpm constant agitation rate in a batch system. Desired amount of FeZn-based nanoparticles were weighed and then mixed with 150 mL dye solutions (AB 29) adjusted to the desired pH values with NaOH and HCl solutions. Samples were taken and centrifuged at specific time intervals (0, 5, 15, 30, 60, 120, 180, 240, 300, 360, 420, 1440, 1500, 1600, 1800, and 2000) in the shaking water bath. Centrifuged samples were diluted and analyzed by using a UV-Vis spectrophotometer at 663 nm wavelength. Dye removal % was determined by the following formula:

$$\text{Dye Removal \%} = \left(\frac{C_0 - C_e}{C_0}\right) \times 100, \quad (1)$$

where C_0 and C_e are the initial and equilibrium dye concetration in $mg{\cdot}L^{-1}$, respectively. The amount of dye adsorbed per unit of the adsorbent at equilibrium was calculated in terms of q_e ($mg{\cdot}g^{-1}$) using the equation given below. The equilibrium amount of dye removal per unit of the nanoparticle was determined in terms of q_e ($mg{\cdot}g^{-1}$) using the following equation.

$$\text{Removal capacity}\left(q_e\right) = \frac{(C_0 - C_e)V}{m}, \quad (2)$$

where V is the volume of dye solution (L) and m is the mass of the adsorbent (g).

2.5. Microorganism Growth and Storage Conditions Used for Determination of Antimicrobial Activity of Nanoparticle. *Bacillus subtilis*, *Klebsiella pneumoniae*, *Escherichia coli*, and *Enterococcus fecalis* bacteria used in determination of the antimicrobial effect of nanoparticle were kindly supplied from Dr. AO Adıgüzel, Faculty of Science, Biology Department, Mersin University, Turkey. For the cultivation, Nutrient Agar Nutrient (NA) and Eosin Methylene-blue lactose sucrose agar (EMB) media were used.

2.6. Determination of Antimicrobial Effect of the Nanoparticle. The diffusion method was used to determine the antimicrobial effect of bacterial cultures. Mueller–Hinton Agar (MHA) was used as a nutrient in this method based on the inhibition of the development of microorganisms in the field where the substance to be tested is diffused in the agar. In this method, at the end of the incubation period, ZnF ($ZnFe_2O_4$) based nanomaterials were added to the open zone (microorganism cannot develop) formation around the holes. The resulting zone diameters were measured in mm. The standard deviation of zone diameters was calculated by performing all tests in 3 repetitions. [10–13].

3. Results and Discussion

3.1. Characterization Studies for ZnF-Based Nanoparticles

3.1.1. SEM Results. SEM analyzes were carried out to determine the morphological characteristics of ZnF-based adsorbent before and after AB 29 dye adsorption. SEM images shown in Figure 1 demonstrate that the synthesized

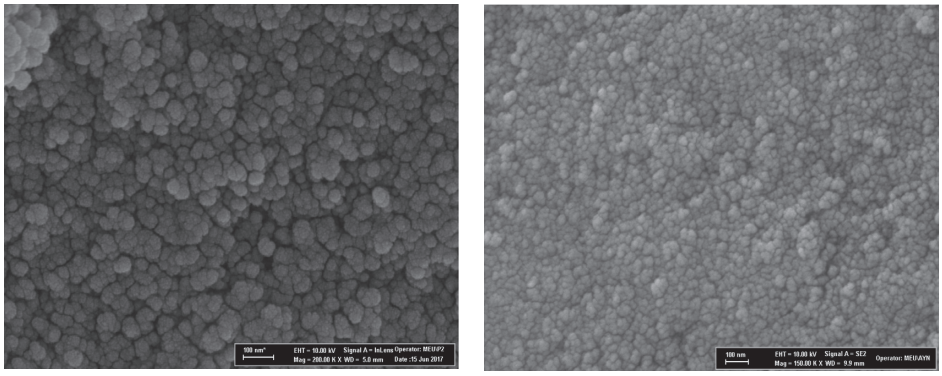

(a) (b)

Figure 1: SEM images for ZnF-based adsorbent (a) before adsorption (b) after adsorption.

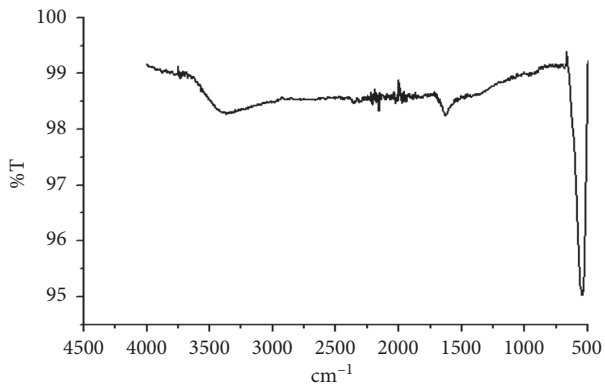

Figure 2: FT-IR spectrum of ZnF-based adsorbent before AB 29 dye adsorption.

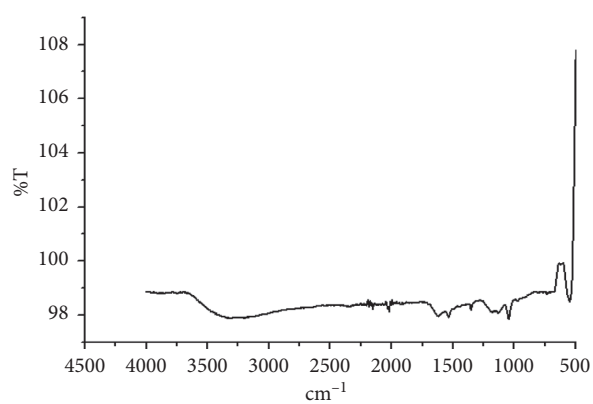

Figure 3: FT-IR spectrum of ZnF-based adsorbent after AB 29 dye adsorption.

material has a bulk structure. It is observed that there are many macropores on the surface of the ZnF-based nanoparticles supplying an evidence about efficient use as an adsorbent.

As it seen from the obtained SEM images, the pores were filled and the surface was filled with dye molecules after

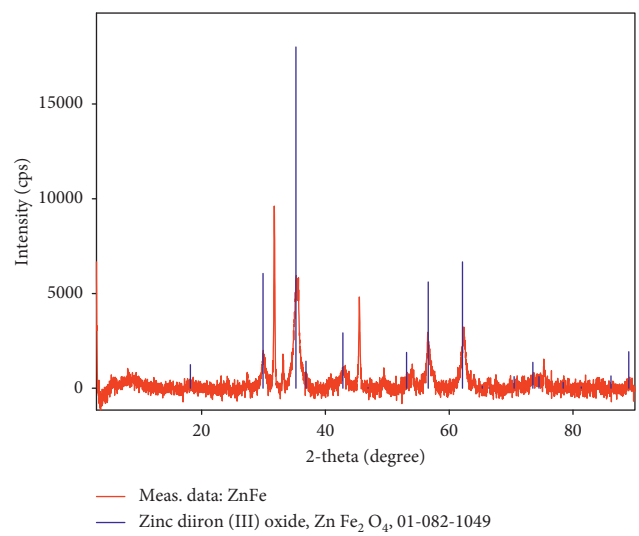

Figure 4: XRD spectrum of ZnF-based adsorbent before adsorption.

removal (Figure 1(b)). Also, from the images, the color removal mechanism is determined as adsorption (agglomerate sizes are about 30 nm and form large structures by connecting to each other) [14].

3.1.2. FTIR Analysis Results. FT-IR analyses were performed to determine the adsorption mechanism of ZnF adsorbent before and after dye adsorption. FTIR studies were conducted to detect the functional organic groups in the adsorbent at a frequency range of 500–4000 cm^{-1}, and Figures 2 and 3 display FTIR spectra of ZnF-based nanomaterials before and after AB 29 dye adsorption.

From Figure 2, it is seen that wide peak of O-H represents stretching vibration at 3450 cm^{-1} and the sharp peak at 500–600 cm^{-1} for Fe-O bond. The slight peak at 1625 cm^{-1} represents OH tension in molecular water. After dye adsorption (Figure 3), a slight peak shifts are observed at all peak ranges as a result of AB 29 adsorption of dye. Also, as a result of AB 29 adsorption of, it is seen that there is an alkoxy C-O bond at 1100 cm^{-1}.

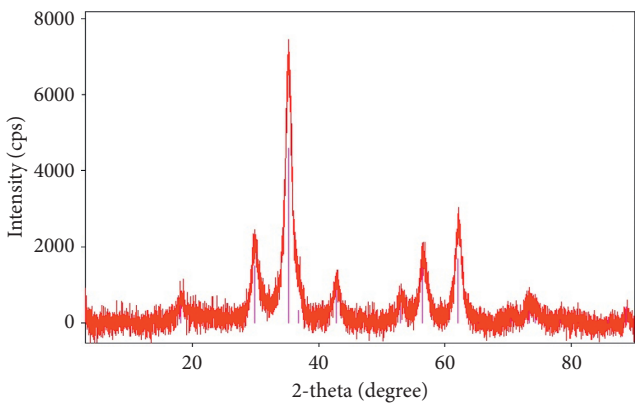

Figure 5: XRD spectrum of ZnF-based adsorbent after AB 29 dye adsorption.

Table 1: The adsorbed dye amount per unit adsorbent mass and removal values % at different initial pH values for AB 29 adsorption to ZnF-based nanomaterials.

pH	q_d (mg·g^{-1})	Removal %
2	98.83 ± 0.97	98.83
3	78.71 ± 0.45	78.71
4	8.74 ± 0.13	8.74
5	2.04 ± 0.03	2.04
6	3.49 ± 0.57	3.49
7	0.58 ± 0.06	0.58
8	1.16 ± 0.12	1.16
9	0.29 ± 0.04	0.29
10	0 ± 0	0

3.1.3. XRD Analysis Results. XRD analysis was carried out to investigate the phases and crystal structure of ZnF-based adsorbent used in AB 29 adsorption. The spectra of the XRD analysis (Figures 4 and 5) are shown below.

From the XRD analysis result, ZnF-based nanomaterials had a cubic crystal structure, and the impurity in the material did not change the cubic crystal structure as shown in Figures 4 and 5 [15]. XRD analysis proved that the simple formula of the material is $ZnFe_2O_4$.

3.2. Batch Adsorption Studies

3.2.1. Initial pH Effect and Isoelectric Point Effect. Initial pH is the most important parameter for color removal from wastewater. In this study, in order to observe the effects of pH parameter on AB 29 adsorption by ZnF-based nanomaterials, pH value was changed between 2.0 and 10.0 range as the initial dye concentration, and temperature and the adsorbent dosage were held constant at 100 mg·L^{-1}, 25°C and 1 g·L^{-1}, respectively.

The adsorbed dye per unit adsorbent mass and removal values % at different initial pH values for adsorption of AB 29 are shown in Table 1.

From Table 1, the favorable pH value for the highest removal efficiency is determined as 2.0. This phenomenon can be explained with isoelectric point. The adsorbent surface was loaded with a positive charge at pH values lower than the determined isoelectric point (pH = 7). Therefore, the electrostatic interaction between the positively charged adsorbent and the dyestuff anions has increased, and as a result, the adsorption capacity of the adsorbent has also increased.

3.2.2. Effect of Initial Dye Concentration. The effect of initial AB 29 dye concentrations on the adsorption by ZnF-based nanomaterials was investigated at an initial pH value of 2.0, temperature of 35°C, and adsorbent concentration of 1.0 g·L^{-1} in the range of 25–2000 mg·L^{-1} dye concentration. From the experimental results, when the initial dye concentration was increased from 25 mg·L^{-1} to 2000 mg·L^{-1} in AB 29 dye adsorption, the adsorbed dye amount in the unit adsorbent mass increased from 25 mg·g^{-1} to 1489.79 mg·g^{-1}, respectively. In AB 29 adsorption process, complete removal was observed at 300 minutes at initial dye concentration of 25 mg·L^{-1}, whereas the adsorption system was observed to reach the equilibrium at 1500 minutes at higher initial dyestuff concentrations.

3.2.3. Temperature Effect. The effect of temperature on the adsorption of AB 29 dye onto ZnF-based nanomaterials was investigated in the AB 29 concentration range and the temperature range of 25–2000 mg·L^{-1} and 25–55°C, respectively, by keeping the initial pH value constant at 2.0, adsorbent concentration of 1.0 g·L^{-1}.

The maximum amount of adsorbed dye per unit adsorbent mass for the adsorption of AB 29 at different temperature values for the equilibrium are shown in Table 2.

According to Table 2, as the temperature increases, there is an increase in adsorbed amounts per unit mass of adsorbent at equilibrium at high concentration levels. From the experimental results, maximum amounts of adsorbed dye per unit ZnF nanoparticle mass were observed at 35°C at high dye concentrations.

When the temperature is increased more than 55°C, the amount of adsorbed dye at equilibrium decreases due to some changes (loss of adsorbent surface activity resulting from temperature degradation of the adsorbent surface) originated in the interior structure of the adsorbent and affect the adsorption yield. This can be attributed to the loss of activity of the adsorbent surface by temperature increase and the degradation of some active sites on the surface by temperature.

3.3. The Effect of Adsorbent. Table 3 shows the effect of the adsorbent concentration on the adsorption of AB 29 by keeping constant the solution pH value of 2.0, initial dye concentration of 100 mg·L^{-1}, and the temperature of 25°C, when the adsorbent concentration are changed from 0.2 to 3.0 g·L^{-1}.

As seen from Table 3, the amount of adsorbed AB 29 by the unit mass of the adsorbent decreases with the increasing adsorbent dose. This is caused that the interaction of the adsorbent particles and agglomeration when the adsorbent dose is increased. From the same table, it is seen that the

Table 2: The maximum amount of dye adsorbed per unit adsorbent mass at different initial temperatures for the adsorption of the AB 29 dye onto ZnF-based nanomaterials.

C_0 (mg·L^1)	q_{max} (mg·g^{-1})			
	25°C	35°C	45°C	55°C
25	25 ± 0	24.56 ± 0.32	24.56 ± 0.28	24.27 ± 0.36
50	49.56 ± 0.19	48.83 ± 0.49	48.25 ± 0.73	48.83 ± 0.58
75	73.39 ± 1.39	72.52 ± 1.90	71.06 ± 1.32	71.64 ± 2.26
100	98.83 ± 0.97	94.75 ± 2.43	89.21 ± 1.36	92.41 ± 2.30
200	154.22 ± 1.95	164.43 ± 2.68	163.84 ± 2.27	150.14 ± 3.44
300	196.79 ± 3.86	219.53 ± 6.56	195.04 ± 3.22	185.13 ± 2.95
400	289.21 ± 4.92	300.87 ± 9.96	271.72 ± 6.69	245.48 ± 3.85
500	371.72 ± 10.17	376.96 ± 19.3	325.65 ± 6.71	285.42 ± 3.99
750	405.97 ± 6.47	557.58 ± 6.21	480.32 ± 17.73	411.80 ± 20.92
1000	755.10 ± 18.90	790.08 ± 12.64	526.23 ± 10.54	537.90 ± 20.58
1500	1132.65 ± 35.29	1155.97 ± 37.06	931.48 ± 21.62	736.15 ± 23.49
2000	1489.79 ± 47.06	1568.51 ± 53.39	1227.40 ± 49.51	976.67 ± 26.48

Table 3: The amount of dye adsorbed per unit mass of the adsorbent and the removal values % at different adsorbent concentrations for adsorption of AB 29 onto ZnF-based nanomaterials.

	AB 29 dye	
X_o (g·L^{-1})	q_d (mg·g^{-1})	Removal %
0.2	164.72 ± 0.34	17.99
0.5	137.01 ± 2.04	43.51
1.0	98.83 ± 0.97	82.00
2.0	49.84 ± 0.87	97.69
3.0	33.33 ± 0	98.53

increase of the adsorbent dose increases the adsorption yield, and it is observed that the color removal is detected as 98.53%, when the amount of adsorbent is 3 g in 1 L.

3.4. Adsorption Equilibrium. In this part of the investigation, linear regression, the best known conventional approach, is used for the determination of the isotherm parameters. For this purpose, Langmuir, Freundlich, and Tempkin isotherm models using the linear transform model (LTFM) are examined. The isotherm constant values are determined from the slope and intercept of the plots of each model equation in linear form. The isotherm parameters for each isotherm model are demonstrated in Table 4 [16, 17].

3.4.1. Langmuir, Freundlich, and Temkin Isotherm Models. Langmuir, Freundlich, and Temkin isotherm model constants were calculated from the plot of each model using the linear transform model (LTFM) and the determined constants and R^2 values are given in Table 4.

As it seen from Table 4, the R^2 values of Langmuir and Frendlich Isotherm models applied to AB 29-ZnF equilibrium data are quite high. According to linear transform model constants, it is determined that AB 29-ZnF adsorption equilibrium data are compatible with the Langmuir and Freundlich isotherm model. When Temkin model regression coefficients are examined for the AB 29 adsorption, it is seen that R^2 values are quite low, so the adsorption system seems to be incompatible with the Temkin model.

Table 4: Langmuir, Freundlich, and Temkin isotherm model constants with regression (R^2) coefficient values.

Langmuir Model				
T (°C)	25	35	45	55
Q° (mg·g^{-1})	303.03	285.71	217.39	277.77
b (L·mg^{-1})	0.4125	0.204	0.273	0.139
R^2	0.841	0.956	0.901	0.946
R_L	0.023	0.046	0.035	0.066
Freundlich Model				
T	25°C	35°C	45°C	55°C
$1/n$	0.3909	0.52	0.47	0.43
n	2.55	1.89	2.09	2.31
K_f ((mg/g)/(L/mg)$^{1/n}$)	13756.25	4138.09	3057.03	3478.56
R^2	0.817	0.937	0.958	0.955
Temkin Model				
T	25°C	35°C	45°C	55°C
A_t (L/g)	0.934	0.77	0.70	0.73
B (J/mol)	291.85	357.42	273.38	220.71
R^2	0.469	0.566	0.603	0.669

3.5. Adsorption Kinetics. In order to investigate the kinetic mechanism of the AB 29-ZnF-based nanoparticle adsorption system, the compatability of the experimental data obtained at different initial dye concentrations to the pseudo-first-order and pseudo-second-order kinetic models was examined [18]. For this purpose, log (q_d–q_t) values versus time graphs for AB 29 dye were plotted, and model rate constants and R^2 (regression coefficient) values from the linearized graph were obtained.

3.5.1. Pseudo-First-Order and Pseudo-Second-Order Kinetic Models. The pseudo-first-order kinetic model parameters obtained for the adsorption of the AB 29-ZnF system are presented in Table 5 with R^2 (regression coefficient) values. From the table, it is seen that the conformity of theoretical values to the experimental ones prove that the adsorption process is not presented with the pseudo-first-order kinetic model.

The pseudo-second-order kinetic model is used to investigate the kinetic mechanism of the AB 29-ZnF adsorption system, and kinetic model rate constants and R^2

Table 5: Pseudo-first-order kinetic model constants and R^2 (regression coefficient) values for adsorption of AB 29 dye on ZnF-based nanomaterials.

C_o (mg·L^{-1})	$q_{d,experimental}$	$q_{d,calculated}$	k_1 (min^{-1})	R^2
25	25	14.77	0.016812	0.963
50	49.56	44.08	0.010824	0.977
75	73.39	61.91	0.006679	0.993
100	98.83	102.42	0.009212	0.991
200	154.22	149.27	0.003455	0.975
300	196.79	214.68	0.003915	0.958
400	289.21	313.40	0.002994	0.979
500	371.72	357.35	0.002533	0.988
750	405.97	363.07	0.003685	0.930
1000	755.10	889.61	0.003915	0.988
1500	1132.65	1249.97	0.002994	0.983
2000	1489.79	1842.46	0.003685	0.985

(regression coefficient) values were determined from the graph of t/q_t versus time at different AB 29 concentrations, as presented in Table 6 [19].

The pseudo-second-order kinetic model supposed that the rate limiting step includes chemisorption of adsorbate on the adsorbent. From Table 6, at all concentrations, pseudo-second-order linear regression correlation coefficients (R^2) were much higher than those of the pseudo-first-order model, and the conformity of theoretical values with the experimental ones prove that adsorption process cannot be represented by the pseudo-first-order kinetic model. This proved that the ZnF adsorption kinetics of AB 29 was not diffusion-controlled [20].

Table 6: Pseudo-second-order kinetic model constants and R^2 (regression coefficient) values for adsorption of AB 29 dye on ZnF-based nanomaterials.

C_0 (mg·L^{-1})	$q_{d,experimental}$	$q_{d,calculated}$	k_2 (g·mg^{-1}·min^{-1})	R^2
25	25	25.12	0.006346	1.00
50	49.56	50.50	0.000736	0.999
75	73.39	75.18	0.000288	0.999
100	98.83	102.04	0.000183	0.998
200	154.22	166.66	4E−05	0.998
300	196.79	212.76	2.67E−05	0.986
400	289.21	333.33	1.01E−05	0.962
500	371.72	416.66	9.52E−06	0.964
750	405.97	476.19	7E−06	0.982
1000	755.10	1000	2.18E−06	0.953
1500	1132.65	1428.57	1.93E−06	0.9538
2000	1489.79	2500	4.19E−07	0.8654

3.6. Adsorption Thermodynamics. Thermodynamic parameters such as Gibbs Free energy change (ΔG), enthalpy change (ΔH), and entropy change (ΔS) values were evaluated according to the Van't Hoff equation to investigate the effect of temperature on the adsorption of AB 29 by ZnF-based nanomaterials [21]. Gibbs free energy change (ΔG), enthalpy change (ΔH), and entropy change (ΔS) values calculated from thermodynamic equations are presented in Table 7.

As it seen from Table 7, the values of Gibbs free energy change (ΔG), enthalpy change (ΔH), and entropy change (ΔS) terms are negative for the AB 29-ZnF adsorption system. This shows that the adsorption process for the AB 29-ZnF system is exothermic ($\Delta H < 0$), spontaneous ($\Delta G < 0$), and stabilized ($\Delta S < 0$) without structural change at the solid/liquid interface [22, 23]. Purkait et al. [24], Iqbal and Ashiq [25], and Karaoğlu et al. [26] have obtained similar thermodinamically adsorption behaviour results in their own investigations.

Table 7: Thermodynamic parameters calculated from the Van't Hoff equation for adsorption of AB 29 dyes on ZnF-based nanomaterials.

T (K)	ΔG (J·mol^{-1})	ΔH (kJ·mol^{-1})	ΔS (J·mol·K^{-1})	$T\Delta S$ (J·mol^{-1})
298	−16704.5			−75536.1
308	−13305.6	−91.96	−253.48	−78070.9
318	−11673.3			−80605.7

3.7. Determination of Antimicrobial Effect of Adsorbent. When the literature is reviewed, it is found that ZnF-based nanomaterials have high antimicrobial property. This part of the investigation is related with the determination of the antimicrobial effect of the ZnF-based nanoadsorbent.

In this experimental part, the antimicrobial properties of ZnF-based nanomaterials produced by the hole agar diffusion method were determined by the cavity diffusion methodology with two different Gram-positive (*Bacillus subtilis* and *Enterococcus fecalis*) and two Gram-negative (*Escherichia coli* and *Klebsiella pneumoniae*) bacteria. The inhibition areas observed as a result of the diffusion susceptibility test are presented in Table 8. The inhibition areas observed for *Bacillus subtilis*, *Enterococcus fecalis*, *Escherichia coli*, and *Klebsiella pneumoniae* bacteria with the susceptibility test are shown in Table 8 (field area size) and in Figure 6 (images).

From the experimental results, it can be said that ZnF-based nanomaterials have antimicrobial property to the antimicrobial effect of four different bacteria at various adsorbent doses. When the experimental data was evaluated, it was seen that the inhibition zones were observed at 25 mg/

Table 8: The inhibition fields observed as a result of the diffusion susceptibility test.

Type of bacteria	Amount of substance (mg·mL^{-1})	Inhibition field diameter (mm)
Bacillus subtilis	25	—
	50	11
	75	15
Enterococcus fecalis	25	—
	50	13
	75	18
Escherichia coli	25	14.5
	50	18
	75	21
Klebsiella pneumoniae	25	—
	50	10
	75	16.5

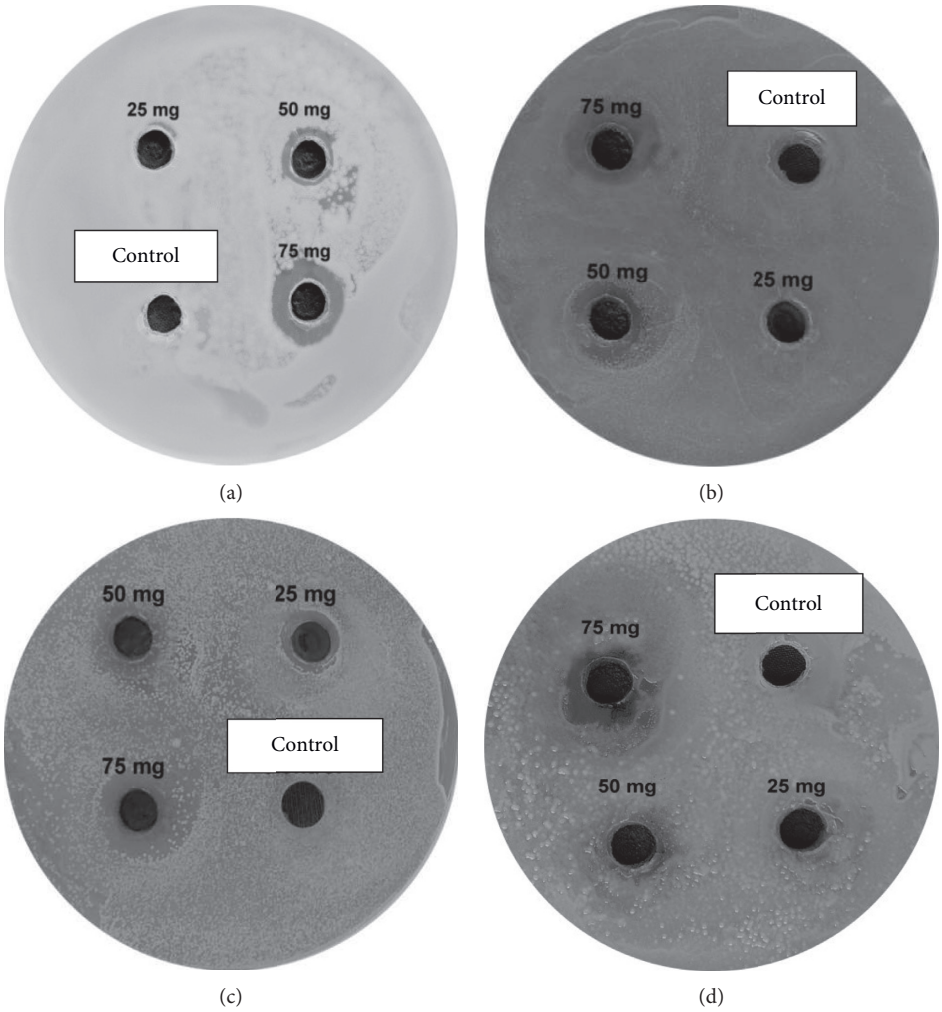

Figure 6: Determination of the antimicrobial effect of ZnF-based nanomaterials on (a) *Bacillus subtilis*, (b) *E. fecalis*, (c) *E. coli*, and (d) *K. Pneumoniae* by the diffusion susceptibility method.

L, 50 mg/L, and 75 mg/L dosages for *E. coli*; at 50 mg/L and 75 mg/L dosages for *Bacillus subtilis* and *Enterococcus fecalis bacteria*; and at 75 mg/L dosage for *Klebsiella pneumoniae bacteremia*.

As a result of the experimental studies, ZnF-based nanomaterials have superior advantage of advanced antimicrobial property against many harmful pathogens besides ecofriendly color removal [26–29].

4. Conclusion

In this investigation, the adsorption of AB 29 dye onto ZnF-based nanomaterials was experimentally researched in a batch system. ZnF-based nanomaterials were synthesized by the coprecipitation method and used for the adsorption of AB 29 dye solution. For the particle characterization, FT-IR was used to identify functional groups in the characterization of the obtained nanomaterials. XRD was used for crystal structure and phase analysis; SEM analyses were performed for surface morphology. As a result of these analyzes, color removal mechanism for the AB 29-ZnF system was determined as adsorption, and the simple formula of the material is detected as $ZnFe_2O_4$. From the antimicrobial effect determination experiments for antimicrobial effect of ZnF-based nanomaterials, it is proved that nanomaterials have advanced antimicrobial property for two different Gram-positive (*Bacillus subtilis* and *Enterococcus fecalis*) and two Gram-negative (*Escherichia coli* and *Klebsiella pneumoniae*) bacteria.

In the other part of the studies, Langmuir, Freundlich, and Temkin isotherm models were applied to the adsorption equilibrium data obtained at different temperatures in the adsorption of AB 29 dye solution onto ZnF-based nanomaterials. It was observed that the equilibrium data of the adsorption process was very compatible with the Langmuir and Freundlich isotherm models.

In order to examine the adsorption kinetics, the kinetic models in the literature were applied to the experimental data for adsorption system. The adsorption data results indicated that the pseudo-second-order kinetic model fitted well the adsorption data of AB 29 onto the ZnF nanoparticles, and it was concluded that the rate limiting step would be chemisorption.

Thermodynamic parameters such as Gibbs free energy change (ΔG), enthalpy change (ΔH), and entropy change (ΔS) were calculated according to the Van't Hoff equation with the help of data obtained at different temperatures. According to experimental results, the AB 29-ZnF system is exothermic ($\Delta H < 0$), spontaneous ($\Delta G < 0$), and stabilized ($\Delta S < 0$) without structural change at the solid/liquid interface.

As a result of the experimental investigation carried out, ZnF-based nanomaterials have superior advantages such as environmental friendliness, antimicrobial character against many harmful pathogens, and simplicity of the synthesis procedure.

In this research, removal of single pollutant (AB 29 textile dye) from synthetically prepared wastewater was investigated by using a novel adsorbent ($ZnFe_2O_4$). However, many different pollutants (heavy metals, phenol, phosphorus, oil, etc.) can be found together in domestic or industrial wastewater at the same time. Thus, taking into account the effects of more than one pollutant, large scale experimental studies for treatment of actual wastewater systems can be achieved. In addition, this study can be proceeded with the help of using a continuous system or more than one reactor to serve the purpose for the high dye removal percentages and reduction of equilibrium time.

Conflicts of Interest

The authors report no conflicts of interest.

Acknowledgments

This investigation was financially sponsored by Mersin University Research Fund Project no. 2017-1-TP2-2266. The authors thank "Mersin University, Department of Scientific Research Projects" "Advanced Technology Education Research and Application Center" for the characterization of the nanoparticle and Dr. A.O. Adıgüzel from Faculty of Science, Biology Department, Mersin University, for the help of the determination for antimicrobial activity of the nanoparticle.

References

[1] J. Rajeev and M. Shrivastava, "Photocatalytic removal of hazardous dye cyanoise from industrial watse using titanium dioxide," *Journal of Hazardous Materials*, vol. 152, pp. 216–220, 2008.

[2] C. C. Chen, A. J. Chaudhary, and S. M. Grimes, "Photodegradation of acid blue 29 and ethyl violet in the presence/absence of sodium hydroxide and aluminum ions," *Journal of Hazardous Materials*, vol. 117, pp. 171–178, 2005.

[3] D. R. Acosta, A. I. Martinez, A. A. Lopez, and C. R. Magana, "Titanium dioxide thin films: the effect of the preparation method in their photocatalytic properties," *Journal of Molecular Catalysis A: Chemical*, vol. 228, no. 1-2, pp. 183–188, 2005.

[4] A. Denizli, R. Say, and Y. Arica, "Removal of heavy metal ions from aquatic solutions by membrane chromatography," *Separation and Purification Technology*, vol. 21, no. 1-2, pp. 181–190, 2000.

[5] S. Arica and V. Singh, "TiO_2 mediated photocatalytic degradation studies of reactive red 198 by UV irradiation," *Journal of Hazardous Materials*, vol. 141, no. 1, pp. 230–236, 2007.

[6] I. A. Alaton, I. A. Balcioglu, and D. W. Bahnemann, "Advanced oxidation of a reactive dyebath effluent: comparison of O_3, H_2O_2/UV-C and TiO_2/UV-A processes," *Water Research*, vol. 36, no. 5, pp. 1143–1154, 2002.

[7] U. Pagga and D. Brown, "The degradation of dyestuffs: part II behaviour of dyestuffs in aerobic biodegradation tests," *Chemosphere*, vol. 15, no. 4, pp. 479–491, 1986.

[8] A. Mittal, J. Mittal, and L. Kurup, "Adsorption isotherms, kinetics and column operations for the removal of hazardous dye, tartrazine from aqueous solutions using waste materials—bottom ash and de-oiled soya, as adsorbents," *Journal of Hazardous Materials*, vol. 136, no. 3, pp. 567–578, 2006.

[9] A. K. Singh, A. Mittal, J. Mittal, and L. Kurup, "Process development for the removal and recovery of hazardous dye erythrosine from wastewater by waste materials-bottom ash and de-oiled soya as adsorbents," *Journal of Hazardous Materials*, vol. 138, no. 1, pp. 95–105, 2006.

[10] V. K. Gupta, A. Mittal, L. Kurup, and J. Mittal, "Adsorption of a hazardous dye, erythrosine, over hen feathers," *Journal of Colloid and Interface Science*, vol. 304, no. 1, pp. 52–57, 2006.

[11] S. Mandal, S. Natarajan, A. Tamilselvi, and S. Mayadevi, "Photocatalytic and antimicrobial activities of zinc ferrite nanoparticles synthesized through soft chemical route: a magnetically recyclable catalyst for water/wastewater

treatment," *Journal of Environmental Chemical Engineering*, vol. 4, no. 3, pp. 2706–2712, 2016.

[12] L. Boyanova, G. Gergova, R. Nikolov et al., "Activity of Bulgarian propolis against 94 *Helicobacter pylori* strains in vitro by agar-well diffusion, agar dilution and disc diffusion methods," *Journal of Medical Microbiology*, vol. 54, no. 5, pp. 481–483, 2005.

[13] S. Alpdoğan, A. O. Adıgüzel, B. Sahan, M. Tunçer, and H. M. Gubur, "Effects of bacteria on CdS thin films used in technological devices," *Materials Research Express*, vol. 4, no. 4, p. 46402, 2017.

[14] R. Sivaraj, P. K. S. M. Rahman, P. Rajiv, H. A. Salam, and R. Venckatesh, "Biogenic copper oxide nanoparticles synthesis using *Tabernaemontana divaricate* leaf extract and its antibacterial activity against urinary tract pathogen," *Spectrochimica Acta Part A: Molecular and Biomolecular Spectroscopy*, vol. 133, pp. 178–181, 2014.

[15] P. Logeswari, S. Silambarasan, and J. Abraham, "Synthesis of silver nanoparticles using plants extract and analysis of their antimicrobial property," *Journal of Saudi Chemical Society*, vol. 19, no. 3, pp. 311–317, 2015.

[16] W. Konicki, D. Sibera, E. Mijowska, Z. Lendzion-Bieluń, and U. Narkiewicz, "Equilibrium and kinetic studies on acid dye acid red 88 adsorption by magnetic $ZnFe_2O_4$ spinel ferrite nanoparticles," *Journal of Colloid and Interface Science*, vol. 398, pp. 152–160, 2013.

[17] C. Muthukumaran, V. M. Sivakumar, and M. Thirumarimurugan, "Adsorption isotherms and kinetic studies of crystal violet dye removal from aqueous solution using surfactant modified magnetic nanoadsorbent," *Journal of the Taiwan Institute of Chemical Engineers*, vol. 63, pp. 354–362, 2016.

[18] Y. E. Boundati, K. Ziat, A. Naji, and M. Saidi, "Generalized fractal-like adsorption kinetic models: application to adsorption of copper on Argan nut shell," *Journal of Molecular Liquids*, vol. 276, pp. 15–26, 2019.

[19] F. Gimbert, N. Morin-Crini, F. Renault, P.-M. Badot, and G. Crini, "Adsorption isotherm models for dye removal by cationized starch-based material in a single component system: error analysis," *Journal of Hazardous Materials*, vol. 157, no. 1, pp. 34–46, 2008.

[20] Y.-J. Tu, C.-F. You, and C.-K. Chang, "Kinetics and thermodynamics of adsorption for Cd on green manufactured nano-particles," *Journal of Hazardous Materials*, vol. 235-236, pp. 116–122, 2012.

[21] O. Długosz and M. Banach, "Kinetic, isotherm and thermodynamic investigations of the adsorption of Ag^+ and Cu^{2+} on vermiculite," *Journal of Molecular Liquids*, vol. 258, pp. 295–309, 2018.

[22] A. Afkhami, S. Sayari, R. Moosavi, and T. Madrakian, "Magnetic nickel zinc ferrite nanocomposite as an efficient adsorbent for the removal of organic dyes from aqueous solutions," *Journal of Industrial and Engineering Chemistry*, vol. 21, pp. 920–924, 2015.

[23] F. Zhang, X. Chen, F. Wu, and Y. Ji, "High adsorption capability and selectivity of ZnO nanoparticles for dye removal," *Colloids and Surfaces A: Physicochemical and Engineering Aspects*, vol. 509, pp. 474–483, 2016.

[24] S. Banerjee and M. C. Chattopadhyaya, "Adsorption characteristics for the removal of a toxic dye, tartrazine from aqueous solutions by a low cost agricultural by-product," *Arabian Journal of Chemistry*, vol. 10, pp. S1629–S1638, 2017.

[25] S. Haciyakupoglu, E. Orucoglu, A. N. Esen, S. Yusan, and S. Erenturk, "Kinetic modeling of selenium (IV) adsorption for remediation of contaminated aquatic systems based on meso-scale experiments," *Desalination and Water Treatment*, vol. 56, no. 5, pp. 1208–1216, 2015.

[26] M. K. Purkait, S. DasGupta, and S. De, "Adsorption of eosin dye on activated carbon and its surfactant based desorption," *Journal of Environmental Management*, vol. 76, no. 2, pp. 135–142, 2005.

[27] M. J. Iqbal and M. N. Ashiq, "Adsorption of dyes from aqueous solutions on activated charcoal," *Journal of Hazardous Materials*, vol. 139, no. 1, pp. 57–66, 2007.

[28] M. H. Karaoğlu, M. Doğan, and M. Alkan, "Kinetic analysis of reactive blue 221 adsorption on kaolinite," *Desalination*, vol. 256, pp. 154–165, 2010.

[29] A. R. Yari, S. Nazari, A. Rastegar, S. Alizadeh-Matboo, G. Majidi, and M. Tanhaye-Reshvanloo, "Removal of acid red 18 dye from aqueous solutions using nanoscale zero-valent iron," *Iranian Journal of Health Sciences*, vol. 3, no. 3, pp. 63–69, 2015.

Hindawi
Journal of Nanotechnology
Volume 2020, Article ID 3683629, 16 pages
https://doi.org/10.1155/2020/3683629

Research Article

Adsorption Capacities of Hygroscopic Materials Based on NaCl-TiO_2 and NaCl-SiO_2 Core/Shell Particles

Marie Bermeo,[1] Nabil El Hadri,[1] Florent Ravaux,[1] Abdelali Zaki,[2] Linda Zou,[2] and Mustapha Jouiad[1,3]

[1]*Department of Mechanical & Materials Science and Engineering, Khalifa University of Science and Technology, Abu Dhabi, UAE*
[2]*Department of Civil Infrastructure and Environmental Engineering, Khalifa University of Science and Technology, Abu Dhabi, UAE*
[3]*Laboratory of Physics of Condensed Mater (LPMC), University of Picardie Jules Verne, Amiens 80039, France*

Correspondence should be addressed to Mustapha Jouiad; mustapha.jouiad@u-picardie.fr

Received 23 September 2019; Accepted 11 December 2019; Published 13 February 2020

Guest Editor: Giorgio Vilardi

Hygroscopic materials which possess high moisture adsorption capacity were successfully upgraded by the functionalization of sodium chloride (NaCl) using two nuances of oxides. A procedure was developed to first prepare submicron-sized NaCl crystals; thereafter, these crystals were coated by choice of either titanium dioxide (TiO_2) or silica (SiO_2) to enhance the hygroscopic properties of NaCl and prevent its premature deliquescence. After coating, several analytical techniques were employed to evaluate the obtained composite materials. Our findings revealed that both composites NaCl-TiO_2 and NaCl-SiO_2 gave excellent performances by exhibiting interesting hydrophilic properties, compared to the sole NaCl. This was demonstrated by both environmental scanning electron microscope (ESEM) and water vapor adsorption experiments. In particular, NaCl-TiO_2 composite showed the highest water adsorption capacity at low relative humidity and at a faster adsorption rate, induced by the high surface energy owing to the presence of TiO_2. This result was also confirmed by the kinetics of adsorption, which revealed that not only does NaCl-TiO_2 adsorb more water vapor than NaCl-SiO_2 or sole NaCl but also the adsorption occurred at a much higher rate. While at room temperature and high relative humidity, the NaCl-SiO_2 composite showed the best adsorption properties making it ideal to be used as a hygroscopic material, showing maximum adsorption performance compared to NaCl-TiO_2 or sole NaCl. Therefore, NaCl-TiO_2 and NaCl-SiO_2 composites could be considered as promising hygroscopic materials and potential candidates to replace the existing salt seeding agents.

1. Introduction

Hygroscopic materials are characterized for their ability to attract and hold water molecules from their surrounding environment. This property has led to numerous applications such as drying agents for moisture-sensitive products (e.g., electronic devices, food, and pharmaceutical products), dehumidifiers, humectants for cosmetic products, adsorbents for industrial adsorption processes [1–4], and aerosols for rain enhancement and water harvesting [5–9]. Sodium chloride (NaCl) is a well-known hygroscopic material which is commonly used as an adsorbent. It is also used as a cloud seeding agent for warm clouds, i.e., hygroscopic cloud seeding, to enhance precipitation due to its affinity towards water [10–13]. Although NaCl and other natural materials are widely used for their good adsorption properties, it remains a challenge to advance the fabrication of new materials with better performances than conventional ones, in terms of two main criteria, namely, higher water uptake and optimum adsorption kinetics at variable conditions of temperature and relative pressure.

In this regard, several complex hygroscopic materials have been developed based on porous materials such as metal-organic framework. For instance, MOF-801 and MOF-841 achieved water adsorption as high as 380 $cm^3\,g^{-1}$ and 550 $cm^3\,g^{-1}$, respectively, at low relative pressure of 0.3, and this performance was evaluated in the temperature range of 15°C to 55°C [14, 15]. Polyacrylamide (PAM) and

sodium polyacrylate (PAAS) are known as superhygroscopic porous materials. They were found to act as a catalyst powder to enhance precipitations with a lower efficiency for PAAS [16]. While other composite adsorbents such as crystalline MCM-41 and calcium chloride ($CaCl_2$) have revealed a high water adsorption capacity of 1.75 kg kg^{-1} in the temperature range of 10–15°C and at 78–92% relative humidity (RH) [17, 18]. Although these materials have very good hygroscopic properties, several factors such as their complex processing routes and their water stability at different conditions of pressure and temperature limit their use especially in cloud seeding.

For cloud seeding applications, the hygroscopic materials need to meet the particle size requirement criterion. According to earlier studies [19–22] based on numerical correlations, modelling, and simulations, the optimum size of seeding materials is in the range of 0.5 to 10 μm in diameter. This particle size range ensures an efficient collision-coalescence process of the cloud condensation nuclei (CCN). This process initiates the water droplet nucleation and enables their growth until they reach the raindrop critical size of about 24 μm in diameter [23]. At this stage, the raindrops may overcome the updraft velocity inside the clouds and be dragged downwards by their own weight to fall as rain [24, 25].

This study concerns the characterization of novel composite materials which were developed through relatively simple mechanisms and using affordable and abundant materials in nature. Here, commercial salt (NaCl) as a raw material was optimized, in terms of size as per cloud seeding requirement, to yield to NaCl crystals with sub-micrometric size. Thereafter, they were coated with thin layers of oxides, either TiO_2 or SiO_2, which have good affinity towards water, i.e., hydrophilicity [26–29], water adsorption [30, 31], and solubility [32–36]. A characterization of the benchmark NaCl particles was carried out to have a baseline reference to be compared to the NaCl-TiO_2 and NaCl-SiO_2 composites obtained after the coating process.

1.1. Hygroscopicity. A hygroscopic solid material can be identified through its hygroscopic point and water uptake capacity. The hygroscopic point ($h_{\text{g.p.}}$) represents the threshold value of the relative humidity in the air above which the solid substance starts adsorbing water vapor [37]. It describes the relationship at equilibrium between the water vapor pressure (P_{sol}) and its surrounding environment with respect to the partial pressure of the water vapor in the air (P_{H2O}) at a specific temperature. $h_{\text{g.p.}}$ is generated as a percentage given by

$$h_{\text{g.p.}} = \left(\frac{P_{\text{sol}}}{P_{\text{H}_2\text{O}}}\right) \times 100\%. \quad (1)$$

If the solid is a water-soluble material such as soluble salts, then P_{sol} represents the water vapor pressure in the solid saturated solution since it already contains a certain amount of moisture at equilibrium prior to saturation. In this case, at the hygroscopic point, the solid material starts experiencing the deliquescence process while adsorbing water vapor from the atmosphere until it starts dissolving rapidly at quasi-constant RH, generally represented by the quasi-vertical line in the isotherm at high RH. This deliquescence property is a characteristic of certain hygroscopic solid compounds, e.g., water-soluble salts, which experience a phase transition from a solid particle to a liquid drop, i.e., to form a solution [38, 39]. Hence, the hygroscopic point of this type of materials at which the deliquescence process occurs is also called deliquescence point or deliquescence relative humidity (DRH) [40–42].

2. Materials and Methods

2.1. Material Synthesis. The chemical compounds were purchased from Sigma-Aldrich with analytical grade. Three types of samples were prepared: (i) optimized neat NaCl with submicron-range particles, (ii) NaCl coated either with titanium dioxide (NaCl-TiO_2), or (iii) silicon dioxide (NaCl-SiO_2). Here, the optimization of NaCl consists of achieving a particle size reduction of commercial NaCl to match the aforementioned size requirements (0.5 to 10 μm) for seeding materials. Herein, an aqueous solution was prepared using commercial salt, and then 1 ml of this solution was added to 50 ml of 2-propanol while stirring. Once a white precipitate is observed, the NaCl crystals were extracted by either centrifugation or filtration, followed by drying in the oven at 80°C. For the synthesis of NaCl-TiO_2 core-shell composite, similar to what was reported by our previous work [43], first TiO_2 solution was prepared by hydrolysis of titanium (IV) butoxide solution as the first step. Solution A was prepared by dispersing 5 ml titanium (IV) butoxide in 40 ml of 2-propanol. Then, solution B was prepared by mixing 50 ml of deionized water and 1 ml of nitric acid. Subsequently, solution B was added dropwise into solution A under vigorous stirring until the formation of a semitransparent TiO_2 solution. A pH control below 2 is crucial to ensure the overall NaCl-TiO_2 particle size in the submicron range. To prepare NaCl-TiO_2 composite, a solution of 50 mg of optimized NaCl and 10 ml of 2-propanol was needed. Then, 1 ml of the above-prepared TiO_2 solution was poured dropwise into this NaCl solution. The new NaCl-TiO_2 solution was stirred vigorously for 60 minutes to be ready for the separation process by centrifugation, drying at 80°C overnight and calcination at 250°C during 3 hours.

For the synthesis of NaCl-SiO_2 core-shell composite, first SiO_2 solution was prepared by the hydrolysis of the tetraethyl orthosilicate (TEOS) solution. An acid solution was prepared by mixing 1.6 ml of hydrochloric acid with 20 ml of ethanol and 20 ml of deionized water. Then, 4.6 ml of TEOS solution was added dropwise into the acidic solution under vigorous stirring. pH was kept at 2 while stirring at 250 rpm for 2 hours. To prepare NaCl-SiO_2 composite, a solution of 50 mg of optimized NaCl and 2 ml of 2-propanol was needed. Then, 1 ml of the above-prepared SiO_2 solution was poured dropwise into this NaCl solution. The new NaCl-SiO_2 solution was stirred vigorously for 60 minutes to be ready for the separation process by centrifugation, drying at 80°C overnight and calcination at 550°C during 3 hours.

2.2. Characterization. Morphology and the size of the synthesized samples were characterized by scanning electron microscopy (SEM), FEI™ Quanta 250, operating at 5 KV, and their elemental composition analysis was determined using energy dispersive X-ray spectroscopy (EDS) from EDAX™. Additional composition analysis was performed using Fourier-transform infrared spectroscopy (FTIR) using a Bruker™ Optics VERTEX system recorded at a wavenumber range of 4000–400 cm^{-1} and Raman spectroscopy from WiTec™ with a laser source of 532 nm. The thin layers of TiO_2 and SiO_2 coating NaCl crystals were revealed by energy-filtered transmission electron microscopy (EFTEM) using GATAN™ and electron energy loss spectroscopy (EELS), energy filter mounted on Titan FEI™ transmission electron microscope (TEM) operating at 300 KV. TEM samples were prepared by dispersion in isopropanol solvent of a powder made of particles and applied to 3 mm Cu grids coated with carbon film.

In situ water vapor condensation was performed by environmental scanning electron microscopy (ESEM) consisting of SEM operating at variable pressure and a gaseous secondary electron detector (GSED) designed for general wet imaging. The *in situ* water condensation setup is shown in Figure 1(a). The condensation experiments were conducted for each sample separately at 10 KV, at variable pressure and at constant temperature of 1°C. To ensure thermal stability on the surface of the sample, cooling at 1°C for a dwell time of 30 minutes was required [44, 45]; thereafter, vapor pressure inside the chamber was increased gradually until the dew point was reached, i.e., formation of water droplets, as per the path shown in the water phase diagram in Figure 1(b). The experimental setup allowed observation of the water droplet nucleation, formation, and growth. The entire water droplet process was then recorded and analyzed frame by frame. The evaluation of the surface wettability and deliquescence of the samples was carried out by the comparison between the diameter of the dried particles under high vacuum and the wet particles during condensation, along with the examination of the altered solid particles after condensation.

A Quantachrome™ Instruments' VSTAR vapor sorption volumetric analyzer was used to record the water adsorption-desorption isotherms, water adsorption capacity, and kinetics of adsorption. The relative pressure (P/P_0) was varied within a range 0–1 equivalent to 0–99% RH. The isosteric heat of adsorption was deduced for each sample from the adsorption isotherms obtained at temperatures of 25°C, 35°C, and 45°C. TA Instruments™ DMA Q800 Dynamic Mechanical Analysis (DMA) in conjunction with a DMA-RH accessory was used to compare qualitatively the mechanical integrity which represents the water adsorption capacity and the deliquescence of the materials. The samples were prepared by compacting the powder samples into a circular disc shape. Water vapor at controlled RH and at equilibrium state was introduced gradually, while the DMA clamp was maintained at a constant compression load of 0.1 N at a room temperature. The result is given as displacements of the clamp in contact with the sample versus RH. The DMA-RH operates from 5 to 90% RH using Peltier elements allowing a precise temperature and RH control of ±0.1°C and ±3% RH, respectively.

3. Results and Discussion

3.1. Morphology and Chemical Composition. Commercial NaCl exhibits random particle sizes mostly greater than 100 μm (Figure 2(a)). To optimize the particle size and to obtain cubic-shaped NaCl particles, a systematic analysis of the agglomerated particles was performed. As a result, a remarkable particle size reduction and individual cubic-shaped NaCl particles arose as an effect of 2-propanol (Figure 2(b)). The optimized NaCl particles obtained by centrifugation have a size ranging from 1 to 6 μm with an average size of 2.3 ± 0.9 μm in length (Figure 2(c)), whereas the ones obtained by filtration have a significantly reduced size ranging from 0.5 and 1.3 μm, with an average size of 0.8 ± 0.2 μm in length (Figure 2(d)). The resultant particle size distribution of the optimized NaCl then appeared to fall within the aforementioned optimum size range for hygroscopic cloud seeding agents as described in the literature [19–22]. Hence, these optimized NaCl particles were used for the coating process.

After the coating process, the morphology and composition of the NaCl-TiO_2 and NaCl-SiO_2 composites were analyzed. SEM micrographs showed uniform particles, i.e., mostly cubic shape and homogeneous size. NaCl-TiO_2 particle sizes ranging from 0.3 to 1.1 μm with an average size of 0.566 ± 0.152 μm in length are the smallest particles achieved (Figure 3(a)). Similarly, an optimum size for NaCl-SiO_2 was obtained with a particle size range between 0.9–6.9 μm and an average of 2.8 ± 1.2 μm in length (Figure 3(b). Furthermore, both composites, NaCl-TiO_2 and NaCl-SiO_2, showed that, during the coating process, the cubic-shaped particles were not destroyed, and they fulfilled the criterion related to the particle size distribution for seeding agents.

EDS elemental composition analysis for the studied samples is represented in Figure 4. A reference EDS spectrum obtained from the optimized NaCl showed Na and Cl peaks (Figure 4(a)), which indicates no contamination during the optimization process. NaCl-TiO_2 composite showed EDS spectra of high peaks of Na and Cl and very small peaks of Ti and O_2 (Figure 4(b)). Likewise, NaCl-SiO_2 composite showed EDS spectra of high peaks of Na and Cl and small peaks of Si and O_2 (Figure 4(c)). In both cases, the EDS composition quantification results indicate that the approximate weight percentage of the oxides in both composites is below 5%.

FTIR analysis revealed the composition of both composites NaCl-TiO_2 and NaCl-SiO_2 (Figure 5). Sole TiO_2 showed FTIR spectra of high absorbance band in the region 500–1000 cm^{-1}, which is certainly due to the bonds between the titanium and the oxygen Ti-O. This is confirmed by the FTIR spectra of the NaCl-TiO_2 composite where the bond Ti-O is present. However, due to the amount of TiO_2 coating in the composite sample (≤5%), the absorbance band observed is significantly low as expected (Figure 5(a)). Similarly, the FTIR spectra of the NaCl-SiO_2 composite showed the presence of three distinctive peaks of low intensity at

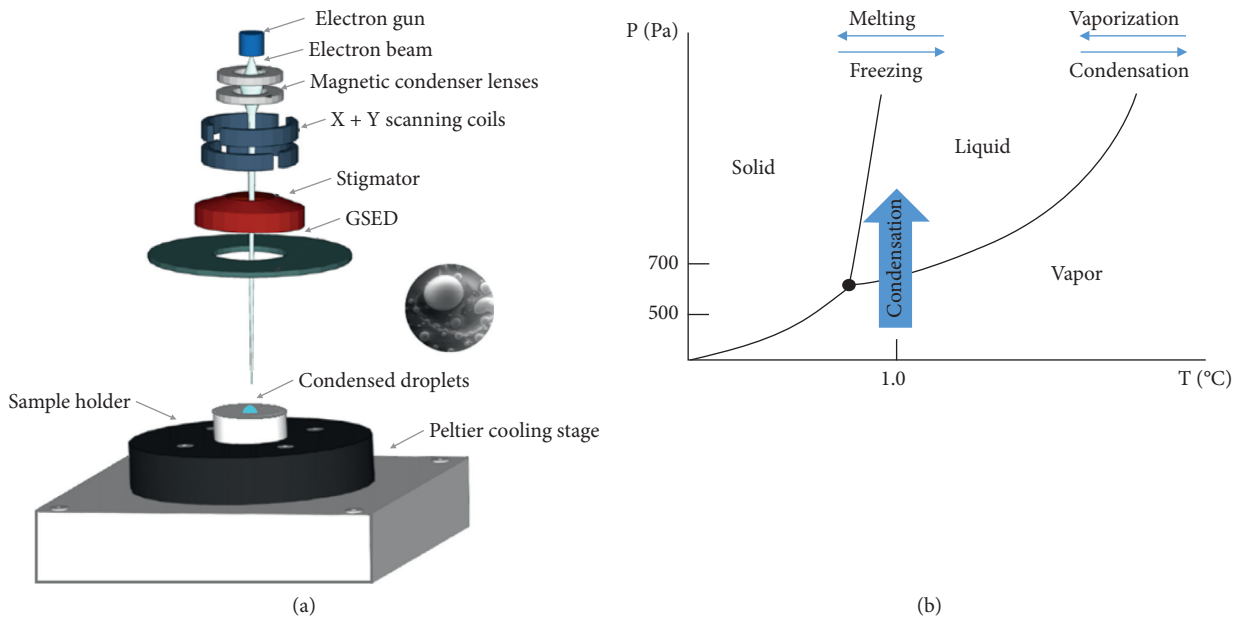

Figure 1: (a) Experimental setup for *in situ* water condensation (ESEM) [42]; (b) water condensation was achieved at a temperature of 1°C and increasing the pressure above 500 Pa.

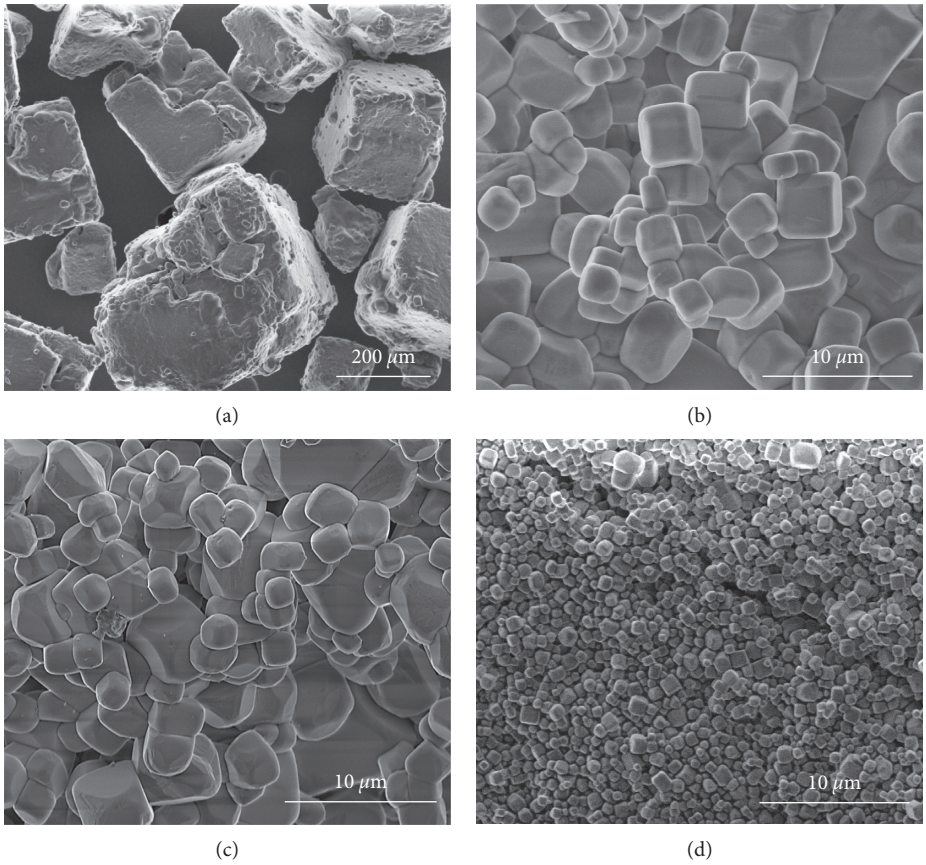

Figure 2: SEM micrographs showing different obtained sizes of NaCl. Sequence 1: (a) commercial NaCl; (b) NaCl after using 2-propanol; and (c) NaCl obtained by centrifugation. Sequence 2: (a) and (b) followed by (d) NaCl obtained after filtration.

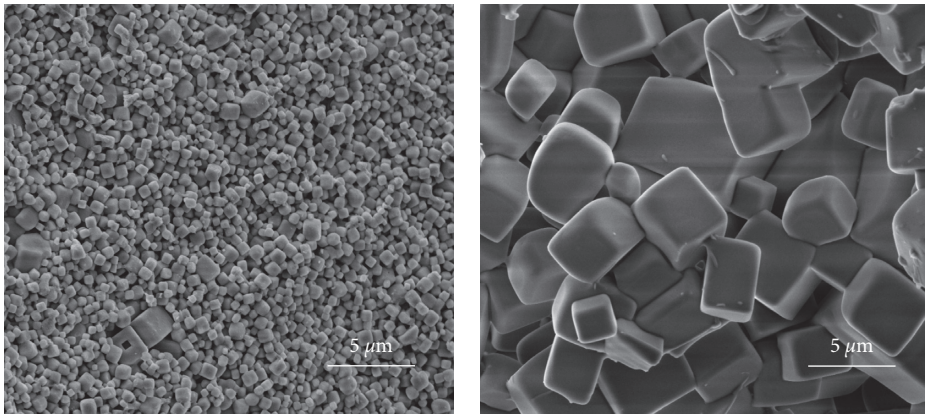

(a) (b)

Figure 3: SEM micrographs of (a) NaCl-TiO_2 and (b) NaCl-SiO_2.

1050 cm^{-1}, 790 cm^{-1}, and 430 cm^{-1} compared to the high absorbance peaks observed for the sole SiO_2 at the same wavenumber (Figure 5(b)).

Additionally, Raman spectroscopy was also used to confirm the characteristic structural fingerprint of the samples NaCl, NaCl-TiO_2, and TiO_2 (Figure 6). As expected, due to the symmetry of NaCl crystals, no Raman signal was detected for NaCl; however, TiO_2 revealed Raman spectra with several peaks in 0–1000 cm^{-1} range and a prominent peak at 152 cm^{-1}. This is a characteristic peak of the anatase phase of TiO_2 [46, 47]. A zoomed-in (inset) figure shows that NaCl-TiO_2 possesses a peak at a Raman shift of 152 cm^{-1}, approximately, which confirms the presence of TiO_2 in the composite material.

Undoubtedly, the oxides TiO_2 and SiO_2 are present in the NaCl-TiO_2 and NaCl-SiO_2 composites, respectively. Hence, in order to verify the quality of TiO_2 and SiO_2 coatings in terms of dispersion and homogeneity, EFTEM and EELS observations were conducted. As a result, an evenly distributed thin layer of TiO_2 on the surface of the NaCl-TiO_2 composite was observed. The TiO_2 coating thickness is approximately 8 nm, which varies slightly from one particle to another (Figure 7).

Likewise, an evenly distributed thin layer of SiO_2 was observed on the surface of the NaCl-SiO_2 composite (Figure 8). The thickness of the coating of SiO_2 surrounding the NaCl particle seems to vary approximately between 8 nm and 12 nm.

For both EFTEM-EELS images, the interaction of the electron beam and the sample creates a shadow effect observed in both images, where the intensity of the thin layer, either Ti or Si, seems to be concentrated in some edges of the particle.

3.2. Water Sorption Analysis. A solid substance is considered as an efficient hygroscopic material when it shows high water adsorption capacity and high rate of adsorption. This is generally the case for porous material possessing high specific surface area or micropore volume, as well as a large pore network [48]. These characteristics can be estimated through the isotherms obtained during the sorption analysis. Besides, the hygroscopic materials being considered as cloud seeding agents are required to exhibit a high-water adsorption capacity especially at low RH and low temperature. Hence, both water adsorption capacity and kinetics of adsorption along with deliquescence are essential parameters to determine the best seeding agent.

In this sense, the hygroscopic properties of the successfully synthesized NaCl-TiO_2 and NaCl-SiO_2 composites compared to neat NaCl were studied to determine their performances under specific conditions. Adsorption isotherms of these materials were obtained at three different temperatures: 25°C, 35°C, and 45°C (Figure 9). The adsorption isotherms exhibited particular performances for all samples in two different stages: at low relative pressure (stage 1), from 0 to 0.6 of relative pressure (i.e., 0 to 60% RH), and at high relative pressure (stage 2), from 0.6 to 1 of relative pressure (i.e., 60 to 99% RH).

At stage 2, multilayer adsorption mechanism and subsequently full deliquescence of the solid adsorbents are reflected on the very steep lines against a very slight increase in relative pressure. The optimized NaCl has comparable water uptakes at all temperatures and a hygroscopic point at approximately 75% RH, which are in accordance with the Extended Aerosol Inorganics Model IV (E-AIM) [49–51] and previous studies [52–56]. The water uptake of neat NaCl above the hygroscopic point at 25°C (3 data points) was correlated to E-AIM as it showed an experimental deviation (Figure 9(a)). Several studies have examined that anatase TiO_2 [27] and amorphous SiO_2 [57–59] exhibit a moderate water uptake as the relative pressure increases. Thus, the steep isotherms of the NaCl-TiO_2 and NaCl-SiO_2 composites at high relative pressure imply that they were boosted by the deliquescence of NaCl (Figures 9(b) and 9(c)).

At stage 1, new graphs were obtained from the full range of relative pressure. These graphs were plotted separately in order to comprehend the adsorption process behavior (Figures 9(d)–9(f)). Here, the temperature seems to be an active kinetics parameter influencing the water uptake at low

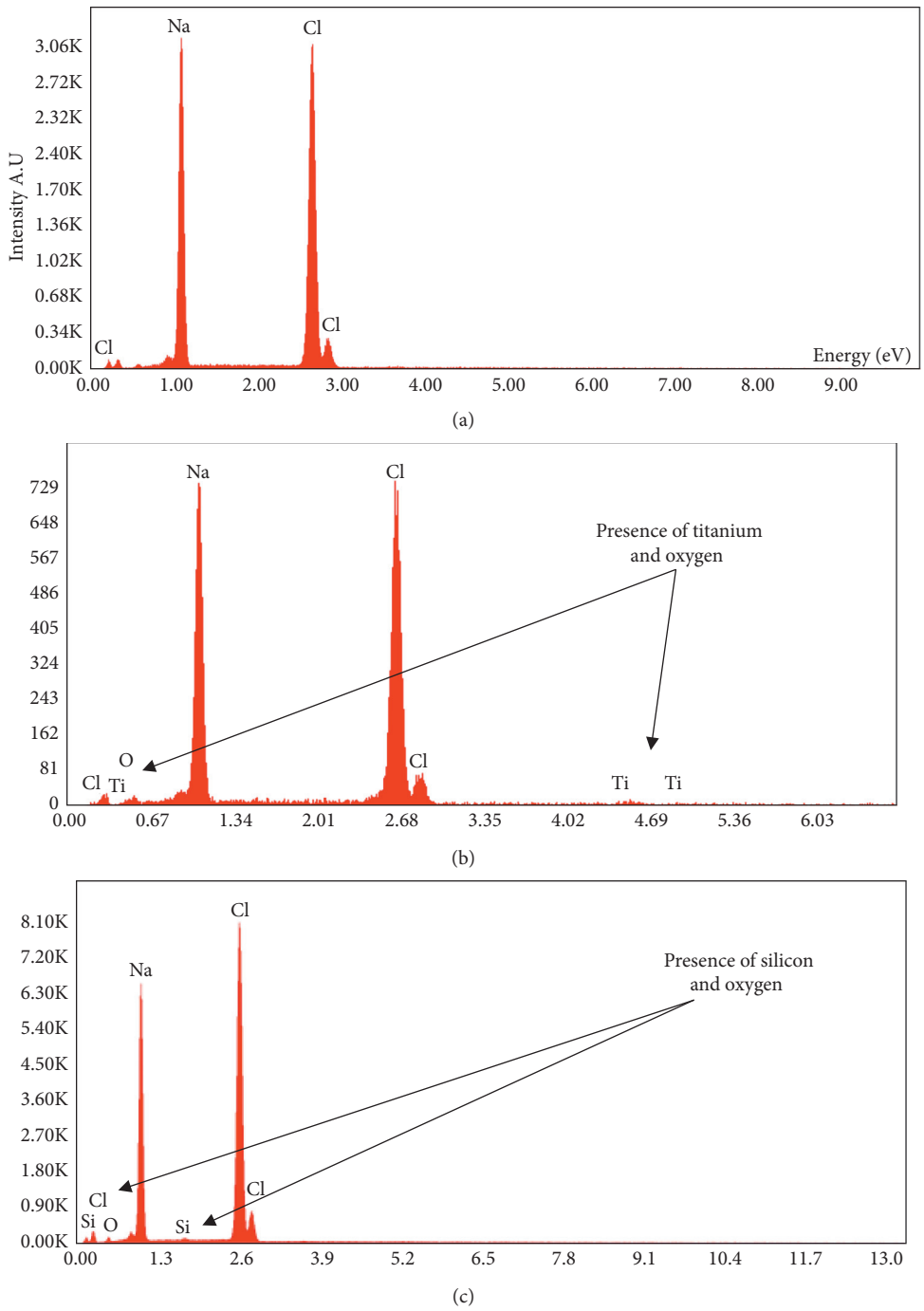

Figure 4: EDS spectra of (a) reduced size NaCl, (b) NaCl-TiO_2, and (c) NaCl-SiO_2.

relatively pressure, even though this stage is related to a monolayer adsorption mechanism. Nevertheless, a similar trend among the samples was observed, i.e., the higher the temperature, the higher the water uptake across the adsorption isotherms. As expected, a slight change in water uptake for NaCl was observed as the relative pressure increases [60–62]. Thus, a nonsignificant influence of NaCl can be inferred on the NaCl-TiO_2 and NaCl-SiO_2 composites at low relative pressure.

The best hygroscopic materials for cloud seeding applications are those capable of adsorbing high amounts of moisture especially at very low relative pressure, i.e., low RH. This is in consideration of the variable pressure profile in the atmosphere and low relative RH, especially in low cloud cover conditions [63, 64]. Accordingly, special attention was given to the analysis of the isotherms at stage 1 (low relative pressure) to evaluate the performances of the samples. Therefore, a comparison of the adsorption isotherms of the

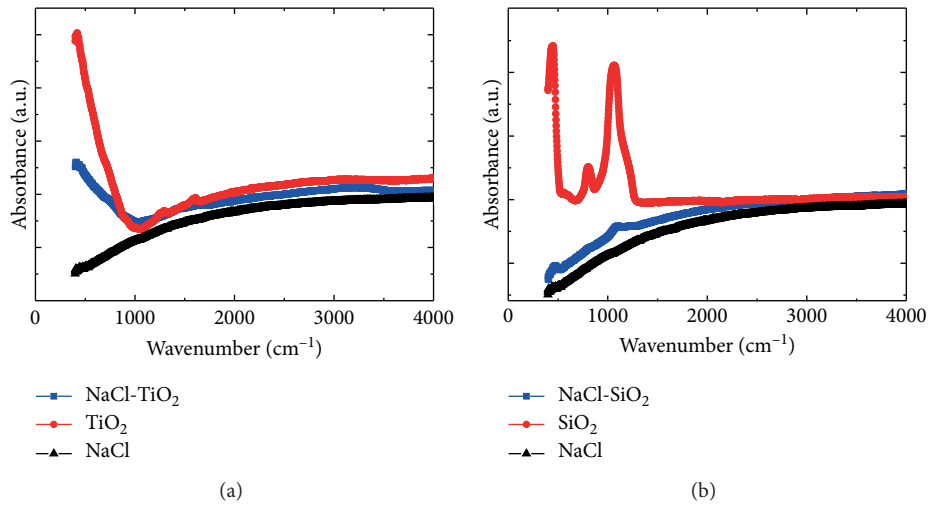

Figure 5: FTIR spectra of (a) NaCl-TiO_2 and (b) NaCl-SiO_2.

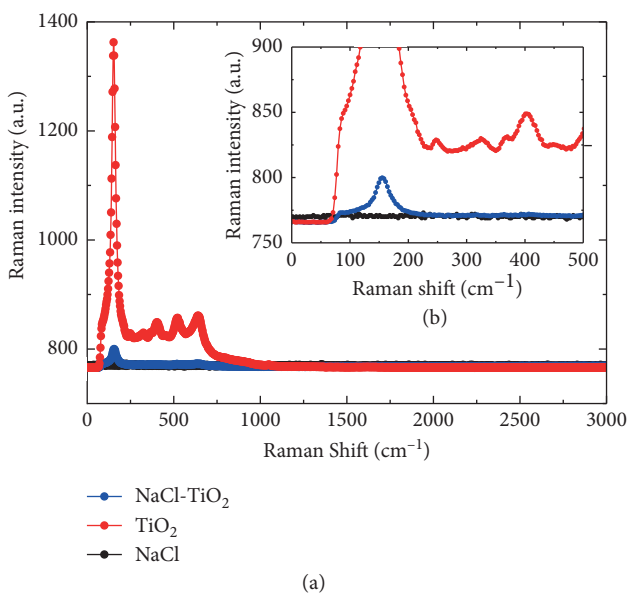

Figure 6: Raman spectra of NaCl, TiO_2, and NaCl-TiO_2. The inert (0 to 500 cm^{-1}) highlights the peak at 152 cm^{-1} approximately, which is the characteristic of TiO_2.

samples were plotted at stage 1 at temperatures of 25°C, 35°C, and 45°C (Figure 10).

According to the IUPAC classification for the adsorption isotherms for gas-solid equilibria [61], at low relative pressure, NaCl-TiO_2 composite followed a sigmoid-shaped isotherm curve, thus reflecting a type IV isotherm. Monolayer-multilayer adsorption attributed to high energy of adsorption is the characteristic of this isotherm [65, 66]. Undoubtedly, NaCl-TiO_2 exhibited the highest water uptake due to the contribution of TiO_2. The surface energy of this oxide facilitates the interaction between the water vapor molecules and the surface of the NaCl-TiO_2. Similarly, NaCl-SiO_2 and NaCl followed the type IV isotherm, but with lower water uptake which indicates less interaction of water molecules with these samples attributed to a minor surface energy of SiO_2 and NaCl, respectively. Overall and for all temperatures, NaCl-TiO_2 shows the highest performance in comparison with NaCl and NaCl-SiO_2. At 25°C, NaCl-TiO_2 showed an increase of water uptake up to 360% with respect to NaCl or NaCl-SiO_2. At 35°C and 45°C, the increase of water uptake reached more than 1000%. Moreover, by increasing the temperature, the water uptake for NaCl-TiO_2 increased from 34.7 mg g^{-1} at 25°C to 140.1 mg g^{-1}at 45°C. These results indicate that TiO_2 significantly enhances the hygroscopicity of the NaCl-TiO_2 composite promoting it as potential candidate for cloud seeding.

At stage 2 (high relative pressure), the effect of the coating on hygroscopicity was not conclusive as it gave mixed results (Figure 11).

It is important to point out that the highest relative pressure at which the maximum water uptake was measured is not accurately 1 (100% RH) for all the samples. The highest relative pressures oscillate in the range of (0.9768–0.9832). As a result, the difference between water uptake at both extreme values of relative pressure may be significant. For example, as per the E-AIM model, NaCl at 25°C (298.15 K) has a water uptake of 24349 mg g^{-1} at 97.68% RH, and 33555 mg g^{-1} at 98.32% RH. Therefore, for close values of water uptake among the samples, the difference may be negligible. At 25°C and 35°C NaCl-SiO_2 and NaCl exhibited higher water uptake than NaCl-TiO_2. At 45°C, an interesting phenomenon occurs. At relative pressure between 0.75 and 0.9, all isotherms overlap; however, above 0.9 relative pressure NaCl-TiO_2 registered the highest water uptake which was above 45000 mg g^{-1} with a clear tendency of increased water uptake with temperature. These results suggest that NaCl-TiO_2 may also be attractive for applications requiring high temperature and high relative pressure. Moreover, although the water uptake of NaCl-SiO_2 has decreased at high temperature, it still reached 30000 mg· g^{-1}, this indicates that NaCl-SiO_2 could be a more suitable hygroscopic material at moderate temperature and high relative pressure, as it reaches its best performance at room temperature.

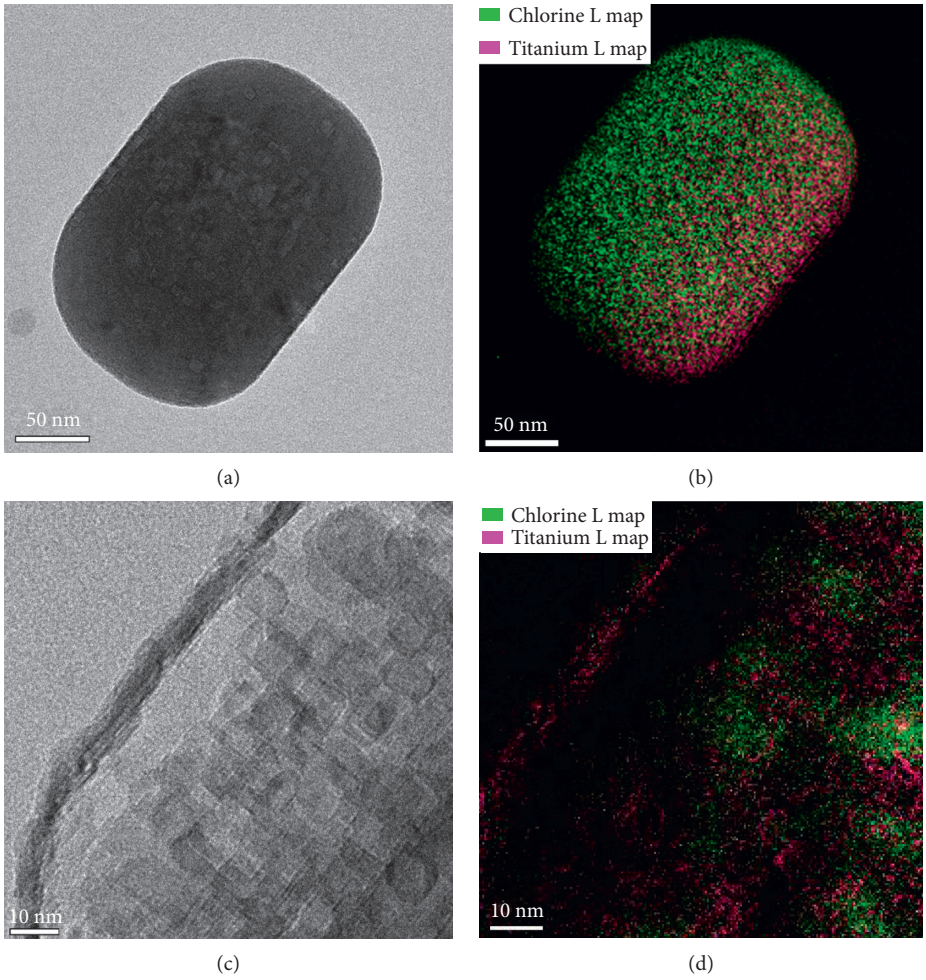

Figure 7: EFTEM-EELS high-resolution images of NaCl-TiO_2: (a, b) one particle of NaCl-TiO_2; (c, d) inset shows the detail of the thickness of TiO_2 surrounding the NaCl particle.

According to the hygroscopicity classification described by Callahan et al. [67] using the concept of equilibrium moisture content (EMC) introduced earlier by Scot et al. [68], the isotherms showed that NaCl-TiO_2 is a very good hygroscopic material, as the water uptake, i.e., equilibrium moisture content or EMC, occurs from very low relative humidity, even below 40% RH, as mentioned in the classification. Although NaCl and NaCl-SiO_2 showed lower water uptake at relative humidity below 70% RH, they are classified as very hygroscopic materials as well because the increase in the EMC is higher than 5% occurring below 60% RH. Another recent classification described by Murikipudi et al. [69] using a different method based on the sorption analysis lead to the same conclusions about these materials classifying them as very good hygroscopic materials.

Additionally, a per the adsorption isotherms at very low relative pressure, the specific surface area for each sample was determined (Table 1). NaCl-TiO_2 exhibited the highest specific surface area which is coherent with its adsorption capacity compared to the other samples. NaCl and NaCl-SiO_2 exhibited similar specific surface areas, which is also consistent with their respective adsorption capacity.

To study the kinetics of water adsorption, the water uptake as a function of time was recorded for each RH (Figure 12). Each point of the plots represents the time that a sample took to reach a maximum water uptake, i.e., water adsorption at equilibrium, at a fixed relative pressure.

The early stages of the water adsorption process are of a major interest because they allow identifying not only the ability of the material to adsorb high quantity of water molecules, but also indicate at which rate the adsorption has occurred. At all temperatures, NaCl-TiO_2 registered faster rate of adsorption and higher water uptake, especially for the first 60 minutes, which is critical for cloud seeding application. It is certain that once the clouds are seeded, rain is expected to fall within the first hour [70]. This interesting characteristic exhibited by NaCl-TiO_2 is attributed to the high energy interaction between the solid adsorbent and water vapor in the presence of TiO_2. For NaCl and NaCl-SiO_2, the kinetics of water adsorption is quite similar, and the adsorption rate is slower in comparison with NaCl-TiO_2. Moreover, the kinetics of adsorption indicates that it depends on temperature. In fact, the water uptake recorded for an equivalent time at equilibrium is higher at 45°C compared to the respective ones at 35°C and 25°C.

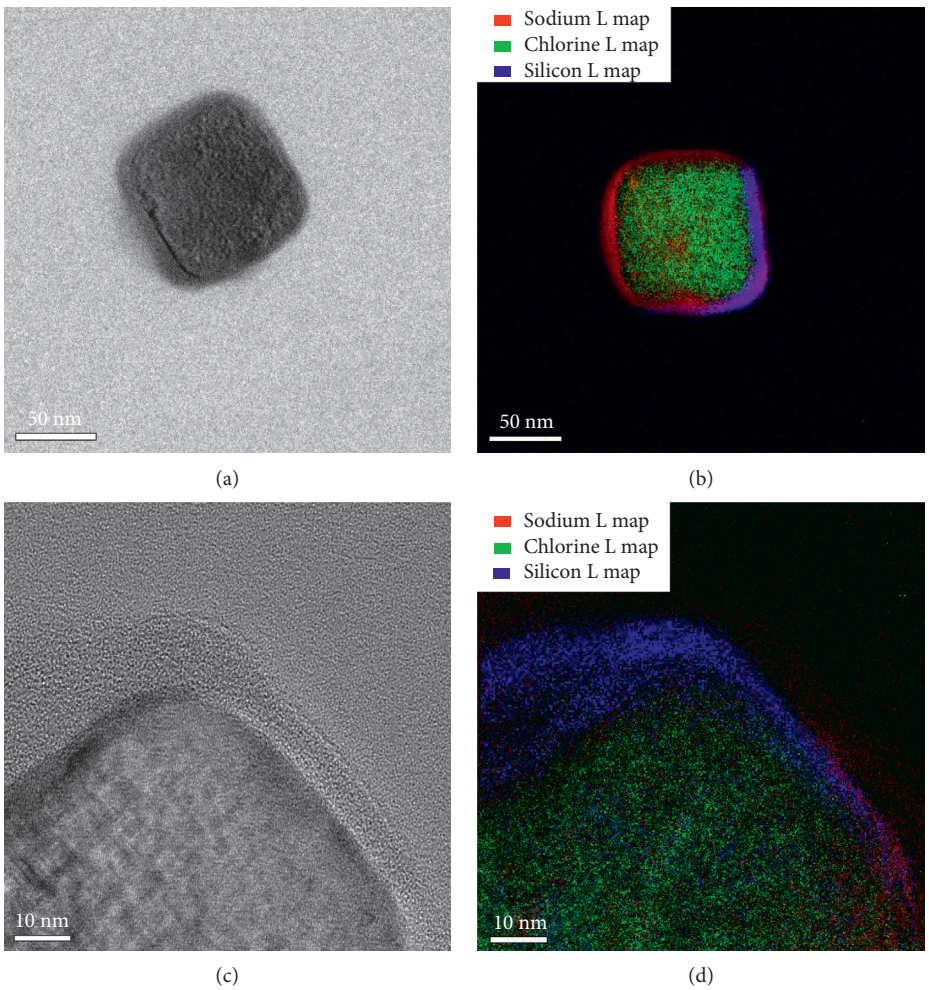

Figure 8: EFTEM-EELS high resolution images of NaCl-SiO_2: (a, b) one particle of NaCl-SiO_2; (c, d) inset shows the detail of the thickness of SiO_2 surrounding the NaCl particle.

In addition, using the adsorption isotherms at various temperatures, the isosteric heat of adsorption can be determined. The isosteric heat of adsorption, also called enthalpy of adsorption (ΔH_{ads}), indicates the strength of the interaction (bond) between the adsorbate (water molecules) and the solid adsorbent [71, 72]. This parameter represents the energy necessary for the heat of vaporization of moisture in a material during the adsorption process to exceed the latent heat of vaporization of pure water at a certain temperature [73]. It is derived from the Clausius–Clapeyron equation [48]:

$$\frac{\delta \ln P}{\delta (1/T)} = \frac{(\Delta H)}{R}, \tag{2}$$

where P is the absolute pressure, T is the temperature, ΔH is the enthalpy of adsorption, and R is the ideal gas constant.

The values of ΔH_{ads} were deduced from the data of pressure and temperature in equilibrium conditions represented by the three isotherms. The results are given as a slope $\Delta H_{ads}/R$ of the plot ln (P) versus (T^{-1}) (Figure 13).

ΔH_{ads} extracted from the plots of Figure 13 is shown in Figure 14. A particular variation of the NaCl-TiO_2 composite was observed. At the beginning of water adsorption, ΔH_{ads} is high around 45.2 kJ·mol^{-1}, and then it drops to 41.4 kJ·mol^{-1}, approximately.

This indicates that the high activity of polar sites on the surface of the solid adsorbent (i.e., high energy interaction) are covered with water molecules to form a monomolecular layer [74, 75], which is consistent with the previous results of the adsorption kinetics obtained for the first 60 minutes, and the significant water uptake at stage 1 (low relative pressure). Moreover, the low values of ΔH_{ads} are due to the progressive and slower filling of the less available sites, known to have lower bonding activation energies [76, 77]. Additionally, those initial values of ΔH_{ads} are higher than the latent heat of vaporization of pure water (43.1 kJ·mol^{-1} at 45°C). At these conditions, the energy of binding between the condensed water molecules and the adsorption sites of the solid adsorbent is higher than the energy of binding between the molecules of pure water that hold them together in the liquid phase, which is favorable for the adsorption process to occur [78, 79].

In the contrast, NaCl-SiO_2 showed high ΔH_{ads}, relatively constant throughout all the water adsorption stages. This can

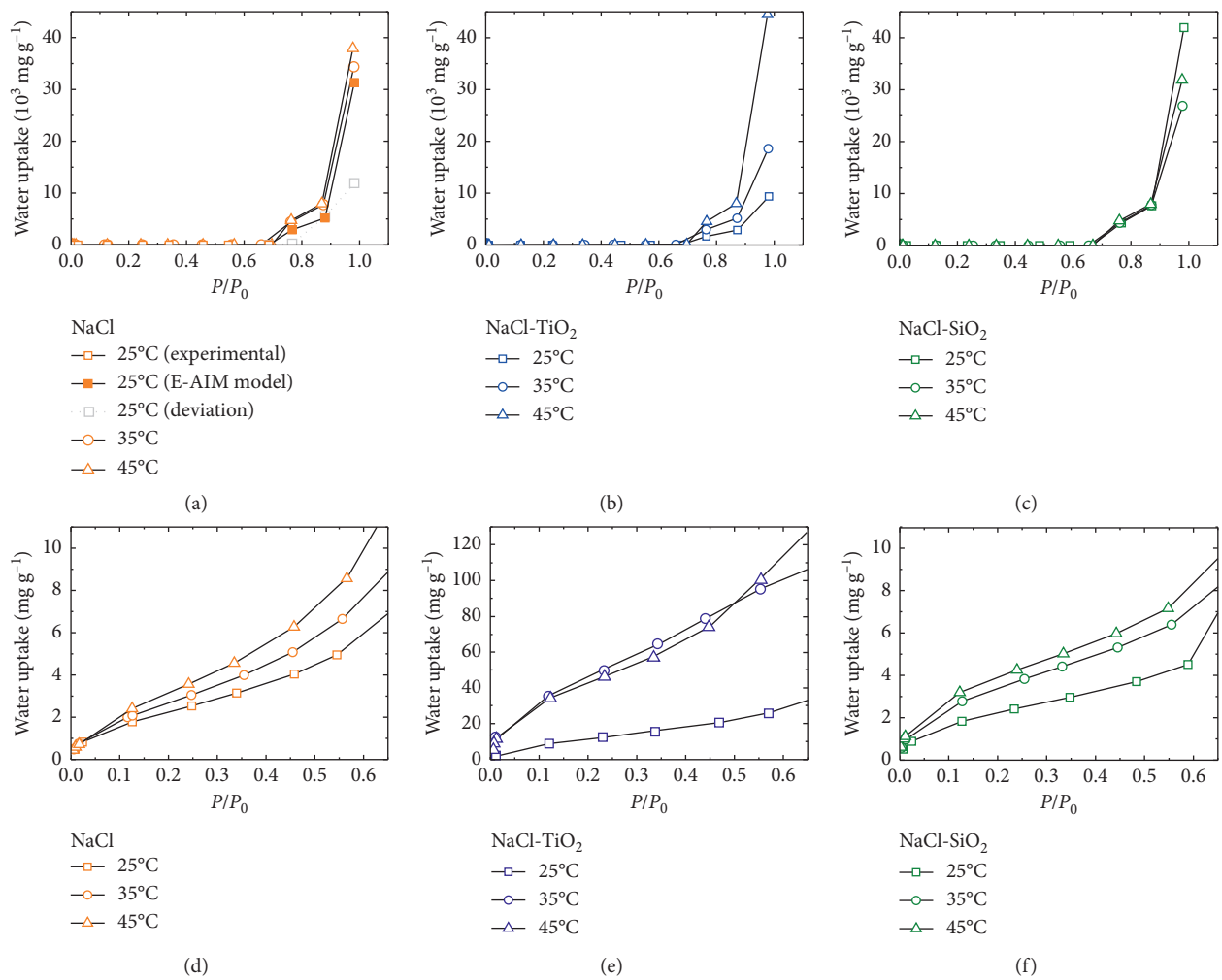

Figure 9: Water sorption analysis with isotherms at 25°C, 35°C, and 45°C: (a) and (d) for NaCl; (b) and (e) for NaCl-TiO_2; and (c) and (f) for NaCl-SiO_2, at relative pressure (0 to 1) top and an inset for low values of relative pressure (0 to 0.6) bottom. The isotherm of NaCl at 25°C shows a deviation obtained experimentally after the hygroscopic point and the correction as per the E-AIM model.

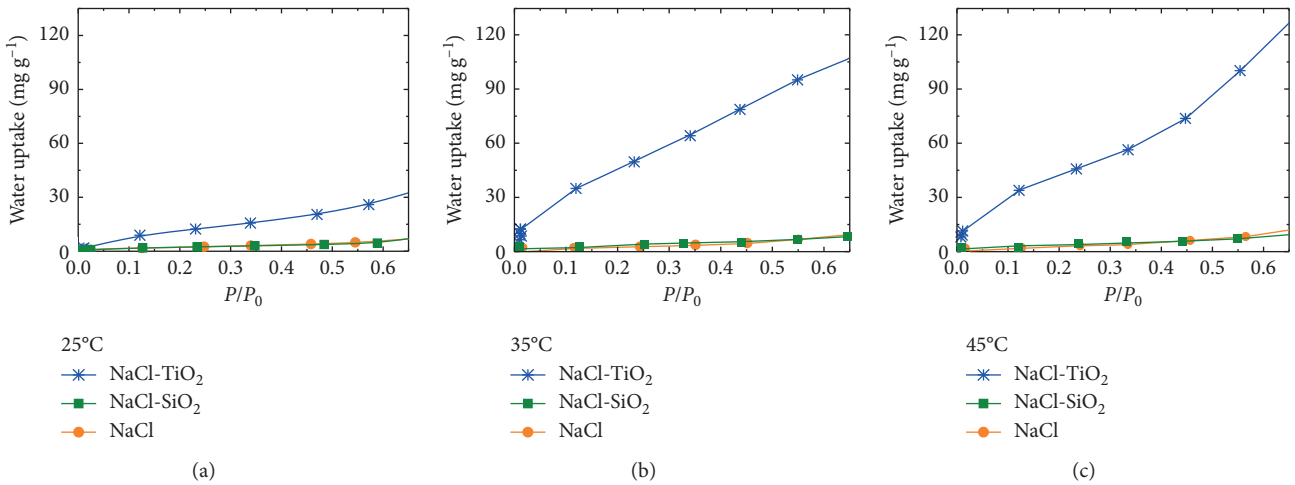

Figure 10: Comparison of isotherms of NaCl, NaCl-TiO_2, and NaCl-SiO_2, at low relative pressure from 0 to 0.7 at (a) 25°C, (b) 35°C, and (c) 45°C.

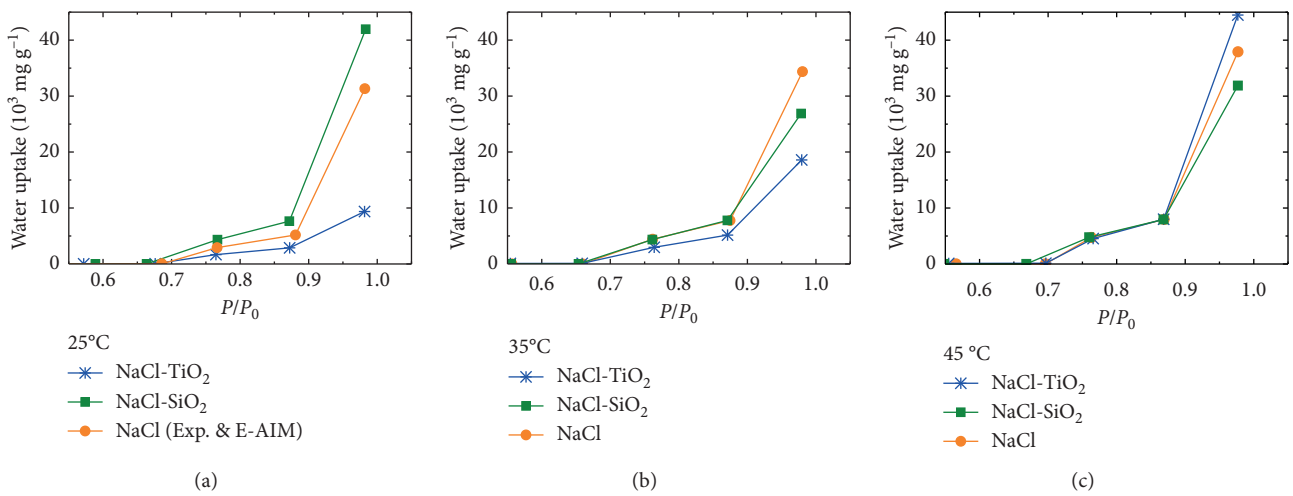

Figure 11: Comparison of isotherms of NaCl, NaCl-TiO_2, and NaCl-SiO_2, at high relative pressure from 0.7 to 1 at (a) 25°C, (b) 35°C, and (c) 45°C. The isotherm of NaCl at 25°C includes the experimental data and the correction as per the E-AIM model after the hygroscopic point as shown in Figure 9(a).

Table 1: Measured specific surface area of NaCl, NaCl-TiO_2, and NaCl-SiO_2 at 25°C, 35°C, and 45°C.

Material	Specific surface area[a] ($m^2 \cdot g^{-1}$)		
	25°C	35°C	45°C
NaCl	9.92	12.05	15.32
NaCl-TiO_2	49.14	201.86	175.30
NaCl-SiO_2	9.83	13.67	15.20

[a]Adsorbate: water vapor. $P/P_0 = 0.05$–0.35.

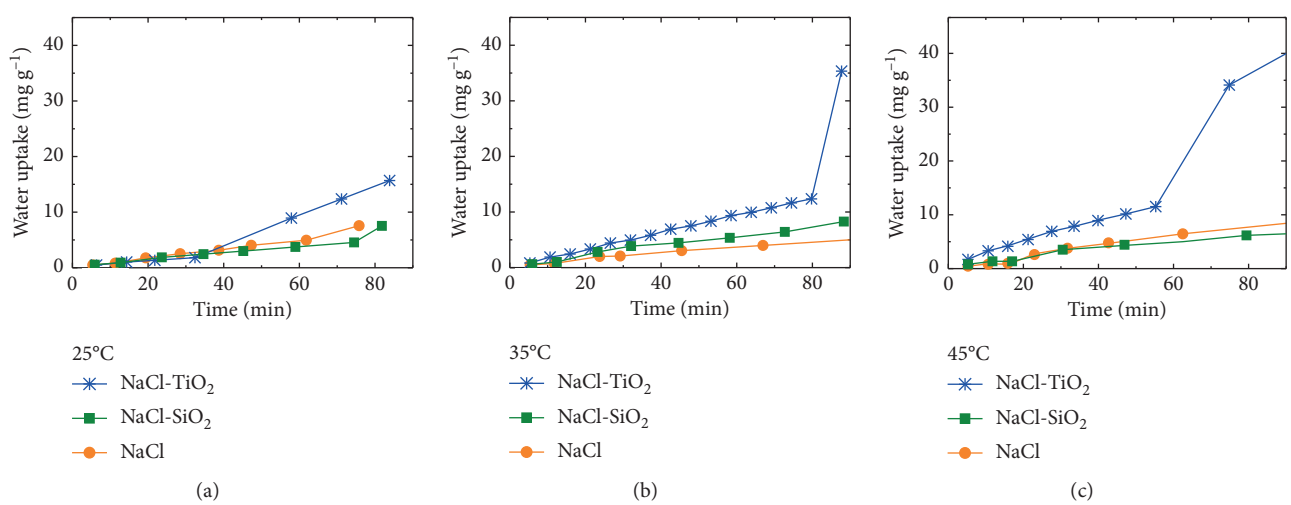

Figure 12: Kinetics of adsorption for NaCl, NaCl-TiO_2, and NaCl-SiO_2 at (a) 25°C, (b) 35°C, and (c) 45°C.

be considered as a valuable behavior in terms of adsorption process. However, NaCl has a slightly mixed trend of the isosteric heat of adsorption: at low water uptake, ΔH_{ads} is slightly above the latent heat of vaporization of pure water, but for high water uptake, up to 6000 mg·g^{-1} approximately, ΔH_{ads} decreases to lower values, and then again, ΔH_{ads} suddenly increases to 42 kJ·mol^{-1} during the last water uptake range. In addition, ΔH_{ads} for NaCl remains lower in all cases than the ones measured or NaCl-SiO_2. This suggests that NaCl-SiO_2 can be considered as a better adsorbent compared to NaCl.

3.3. Wettability Analysis. The water affinity of the samples was analyzed through *in situ* water condensation using ESEM (Figure 15).

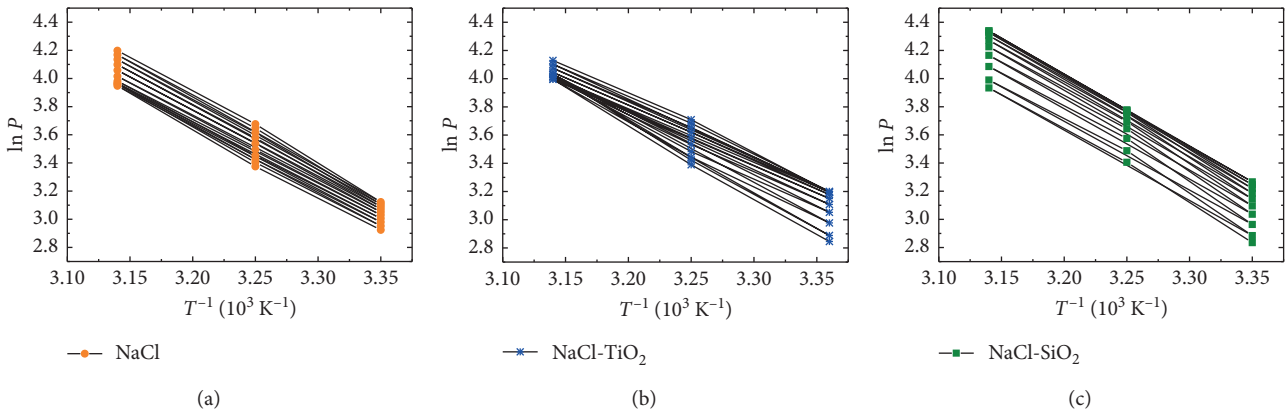

Figure 13: Variation of ln (P) vs. (T^{-1}) of (a) NaCl, (b) NaCl-TiO$_2$, and (c) NaCl-SiO$_2$.

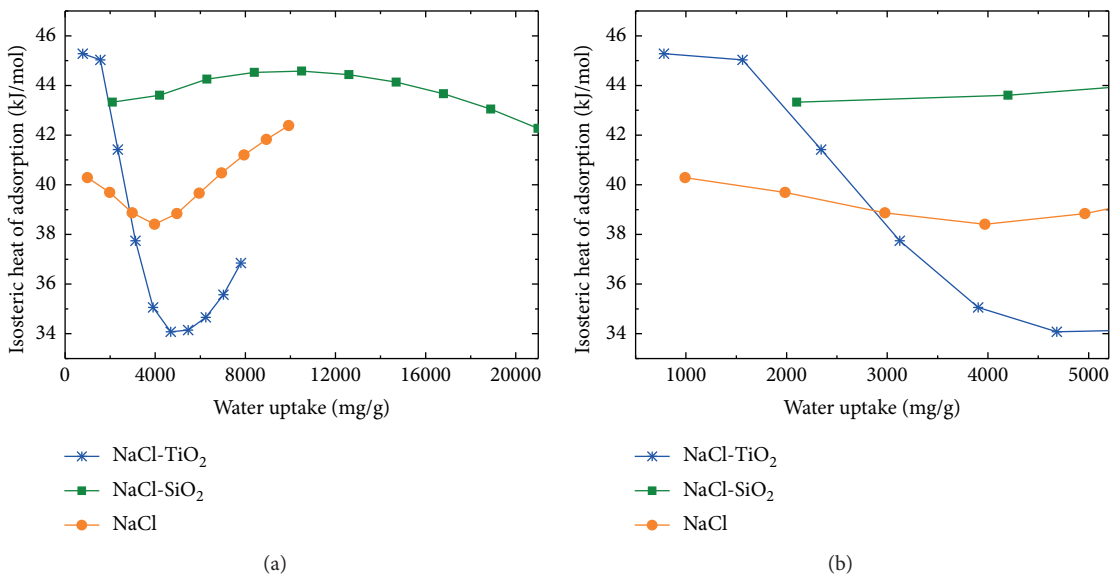

Figure 14: Isosteric heat of adsorption (ΔH_{ads}) of NaCl, NaCl-TiO$_2$, and NaCl-SiO$_2$: (a) full scale; (b) the inset shows the range 500–5000 mg·g^{-1}.

Since the surface wettability of these particles is the major interest to determine the extent of hydrophilicity and deliquescence, individual particles were analyzed. The pressure was increased gradually until the nucleation of the first water droplets was observed. At equilibrium, the water droplets stopped growing, while the pressure was still increasing, i.e., the water droplets reached their maximum diameter which represents the maximum water adsorption capacity. The diameter of the droplets was then measured and compared for the three types of samples. The final step consisted of reducing the pressure gradually until dried samples were observed, i.e., no more physical changes in the remaining particles. This last step clarified the understanding of the effect of the deliquescence process. Both NaCl-TiO$_2$ and NaCl-SiO$_2$ composites have developed larger water droplets compared to neat NaCl. D/D_0, which defines the ratio between the maximum diameter reached by the water droplet at equilibrium to the length of the solid particle, was determined to be ≈3.44, ≈3.76, and ≈2.26 for NaCl-TiO$_2$, NaCl-SiO$_2$, and NaCl, respectively. This indicates that both composite samples are more hydrophilic in nature than NaCl. It is noteworthy to emphasizing that the *in situ* condensation experiments at low temperature and pressure emulate the water vapor condensation process in the clouds with a close approximation, specifically, in warm clouds which are the main target for hygroscopic cloud seeding. Furthermore, once the condensation is achieved, the moisture was gradually removed until the particles are dried. The results showed that the size of neat NaCl remained relatively unchanged after the condensation experiments which suggests that both slow adsorption and a limited deliquescence process have occurred during the course of the experiment for neat NaCl. In contrast, after the condensation experiments, both composites NaCl-TiO$_2$ and NaCl-SiO$_2$ turned to a dispersed fine powder or they were entirely disintegrated which indicates a good deliquescence.

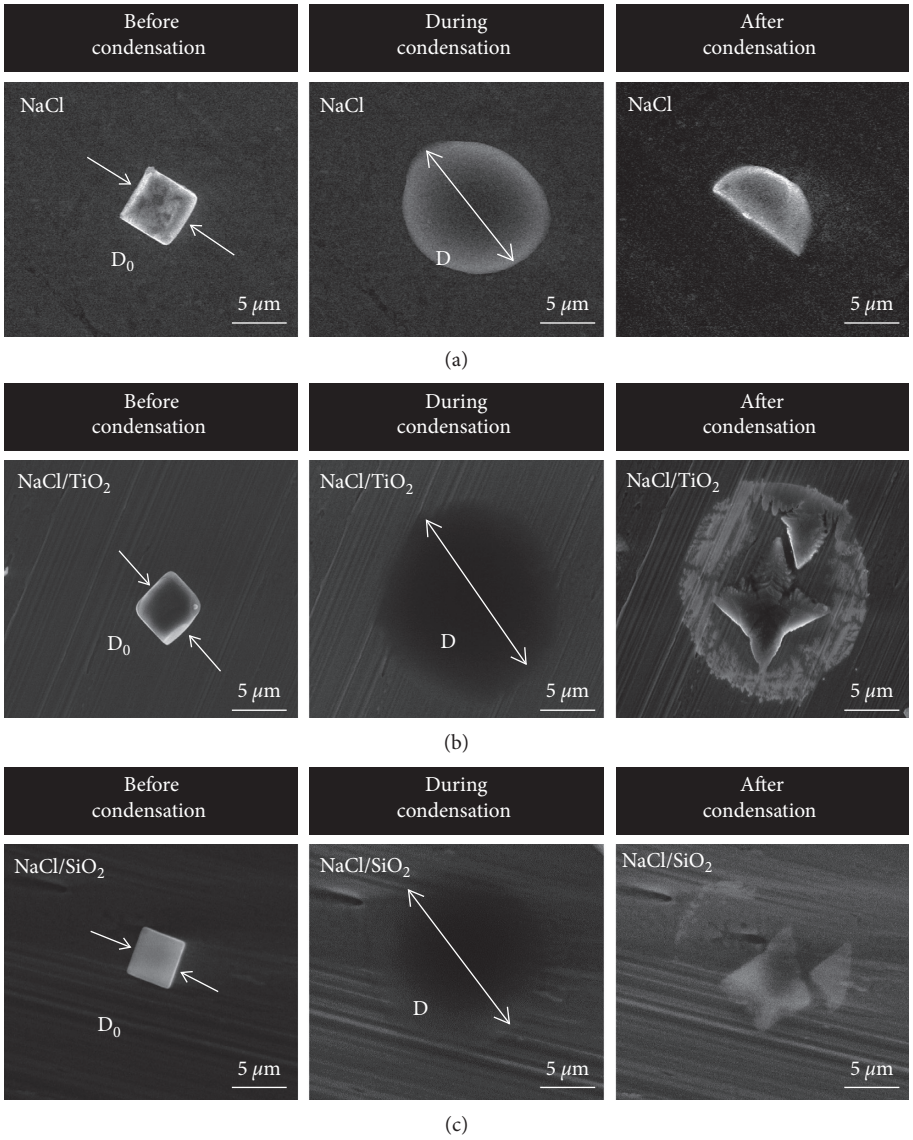

Figure 15: *In situ* condensation experiments inside ESEM at three key stages before condensation (left: dry samples); during condensation (center: samples at equilibrium), and after condensation (right: dried sample after water is removed) performed, respectively, on (a) NaCl (b) NaCl-TiO_2, and (c) NaCl-SiO_2.

Therefore, these results allowed to infer that both composites adsorb more water and deliquesce more effectively than neat NaCl.

3.4. Humidity-Controlled Dynamic Mechanical Analysis (DMA-RH). DMA-RH results are illustrated in Figure 16. Two stages can be identified: in stage 1, from 0 to 50–70% RH, the materials showed a distinctive water uptake related to an initial swelling and a subsequent softening of the area in contact with the DMA clamp. Thus, a negative displacement due to the penetration of the clamp inside the disc-shaped samples is recorded, while the moisture is increased in the chamber. In stage 2, from 50–70% RH to 90% RH, approximately, the materials experienced a steeper negative displacement since the clamp load has overcome the resilience of the materials which became softer due to the high amount of water adsorbed. At this stage, samples are deformed or dispersed. This behavior can be linked to the deliquescence process of the solid particles in water as seen in ESEM experiments and the isotherms.

NaCl presents no measurable water uptake at low relative humidity (stage 1). This is interpreted by a minor displacement as observed on the DMA-RH plot. At high RH (stage 2), a large displacement is recorded, and the deliquescence seemed to occur at 50–65% RH, where a sudden drop of the curve was observed. In contrast, the NaCl-TiO_2 composite started adsorbing water at the very beginning of RH (stage 1), and a significant displacement is recorded which stabilized and formed a plateau up to 60% RH, and then a rapid drop was observed in the range of 60–75% RH, at which the NaCl-TiO_2 composite deliquesces (stage 2). This indicates that

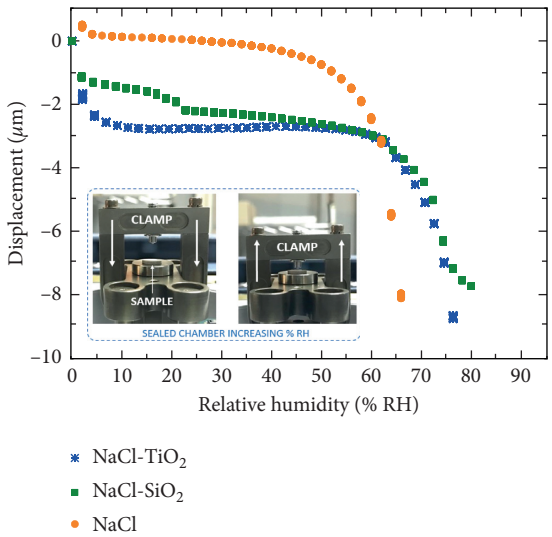

Figure 16: Humidity-controlled dynamic mechanical analysis of NaCl, NaCl-TiO_2, and NaCl-SiO_2.

NaCl-TiO_2 retained higher amount of moisture compared to NaCl. Moreover, NaCl-SiO_2 exhibited 3 stepwise water uptakes ranging from 0 to 20% RH as step 1, ranging from 20 to 60% RH as step 2, and starting above 60% RH as step 3 which suggests a multilayer adsorption. This indicates that NaCl-SiO_2 is behaving like NaCl-TiO_2 in terms of water uptake but at lower kinetics as NaCl-SiO_2 needs two stages of adsorption at low relative pressure to achieve similar water uptake than NaCl-TiO_2. Both water uptake curves showed that NaCl-SiO_2 deliquesces approximately at the same relative humidity as NaCl-TiO_2 (60 to 75% RH). Therefore, the two composites, NaCl-TiO_2 and NaCl-SiO_2, have demonstrated better water adsorption and deliquescence compared to NaCl but at higher rate for NaCl-TiO_2.

4. Conclusions

The successful optimization in terms of size and morphology of the commercial NaCl as per cloud seeding requirements allowed the development of the NaCl-TiO_2 and NaCl-SiO_2 composites. The effective coating process of NaCl preserved the cubic-shaped particles and size (0.5 to 6.9 μm) as per cloud seeding agent requirements.

Water adsorption analysis revealed that the NaCl-TiO_2 composite adsorbed high amount of water vapor at a faster rate in the cloud seeding conditions (low relative pressure) compared to NaCl and NaCl-SiO_2. In addition, NaCl-TiO_2 exhibited very promising adsorption properties for high-temperature applications as high as 45°C. Moreover, NaCl-SiO_2 was found to be potentially suitable hygroscopic material for high relative pressure applications while reaching its highest performance at room temperature.

In situ water condensation inside the ESEM and the DMA-RH tests confirmed that NaCl-TiO_2 composite possesses the best performances in terms of water adsorption capacity and deliquescence compared to NaCl. Likewise, NaCl-SiO_2 showed a comparable behavior as NaCl-TiO_2 but at lower kinetics.

Therefore, both composites NaCl-TiO_2 and NaCl-SiO_2 could be considered as promising hygroscopic materials and as potential candidates to replace the existing salt seeding agents for rain enhancement.

Data Availability

The (SEM and TEM images, the movies of the *in situ* ESEM, and the graphs) data used to support the findings of this study are available from the corresponding author upon request.

Conflicts of Interest

The authors declare that there are no conflicts of interest regarding the publication of this paper.

Acknowledgments

The financial support was provided by the National Center of Meteorology and Seismology, Abu Dhabi, UAE, under the UAE Research Program for Rain Enhancement.

Supplementary Materials

Water vapor adsorption kinetics of coated and uncoated NaCl: inset is an illustration of the adsorption among samples. (*Supplementary Materials*)

References

[1] J. U. Keller and R. Staudt, *Gas Adsorption Equilibria: Experimental Methods and Adsorptive Isotherms*, Springer Science & Business Media, Berlin, Germany, 2005.

[2] M. N. Golubovic, H. D. M. Hettiarachchi, and W. M. Worek, "Sorption properties for different types of molecular sieve and their influence on optimum dehumidification performance of desiccant wheels," *International Journal of Heat and Mass Transfer*, vol. 49, no. 17-18, pp. 2802–2809, 2006.

[3] X. Zheng, T. S. Ge, R. Z. Wang, and L. M. Hu, "Performance study of composite silica gels with different pore sizes and different impregnating hygroscopic salts," *Chemical Engineering Science*, vol. 120, pp. 1–9, 2014.

[4] S. Yildirim, B. Röcker, M. K. Pettersen et al., "Active packaging applications for food," *Comprehensive Reviews in Food Science and Food Safety*, vol. 17, no. 1, pp. 165–199, 2018.

[5] R. T. Bruintjes, "A review of cloud seeding experiments to enhance precipitation and some new prospects," *Bulletin of the American Meteorological Society*, vol. 80, no. 5, pp. 805–820, 1999.

[6] G. K. Mather, D. E. Terblanche, F. E. Steffens, and L. Fletcher, "Results of the South African cloud-seeding experiments using hygroscopic flares," *Journal of Applied Meteorology*, vol. 36, no. 11, pp. 1433–1447, 1997.

[7] Y. Tu, R. Wang, Y. Zhang, and J. Wang, "Progress and expectation of atmospheric water harvesting," *Joule*, vol. 2, no. 8, pp. 1452–1475, 2018.

[8] K. R. Spurny, "Atmospheric condensation nuclei P. J. Coulier 1875 and J. Aitken 1880 (historical review)," *Aerosol Science and Technology*, vol. 32, no. 3, pp. 243–248, 2000.

[9] D. M. Chate, P. S. P. Rao, M. S. Naik, G. A. Momin, P. D. Safai, and K. Ali, "Scavenging of aerosols and their chemical species by rain," *Atmospheric Environment*, vol. 37, no. 18, pp. 2477–2484, 2003.

[10] M. Ćurić and D. Janc, "Wet deposition of the seeding agent after weather modification activities," *Environmental Science and Pollution Research*, vol. 20, pp. 6344–6350, 2013.

[11] R. R. Czys and R. Bruintjes, "A review of hygroscopic seeding experiments to enhance rainfall," *The Journal of Weather Modification*, vol. 26, pp. 41–52, 1994.

[12] B. A. Silverman, "A critical assessment of hygroscopic seeding of convective clouds for rainfall enhancement," *Bulletin of the American Meteorological Society*, vol. 84, no. 9, pp. 1219–1230, 2003.

[13] R. T. Bruintjes, V. Salazar, T. A. Semeniuk, P. Buseck, D. W. Breed, and J. Gunkelman, "Evaluation of hygroscopic cloud seeding flares," *The Journal of Weather Modification*, vol. 44, pp. 69–94, 2012.

[14] H. Furukawa, F. Gándara, Y.-B. Zhang et al., "Water adsorption in porous metal-organic frameworks and related materials," *Journal of the American Chemical Society*, vol. 136, no. 11, pp. 4369–4381, 2014.

[15] H. Kim, S. Yang, S. R. Rao et al., "Water harvesting from air with metal-organic frameworks powered by natural sunlight," *Science*, vol. 356, no. 6336, pp. 430–434, 2017.

[16] H. X. Zhu, X. D. Li, and R. J. Yang, "A novel catalyst of warm-cloud seeding to enhance precipitation," *IOP Conference Series: Materials Science and Engineering*, vol. 137, Article ID 012002, 2016.

[17] J. G. Ji, R. Z. Wang, and L. X. Li, "New composite adsorbent for solar-driven fresh water production from the atmosphere," *Desalination*, vol. 212, no. 1-3, pp. 176–182, 2007.

[18] D. Kumar, K. Schumacher, C. du Fresne von Hohenesche, M. Grün, and K. K. Unger, "MCM-41, MCM-48 and related mesoporous adsorbents: their synthesis and characterisation," *Colloids and Surfaces A: Physicochemical and Engineering Aspects*, vol. 187-188, pp. 109–116, 2001.

[19] Y. Segal, A. Khain, M. Pinsky, and D. Rosenfeld, "Effects of hygroscopic seeding on raindrop formation as seen from simulations using a 2000-bin spectral cloud parcel model," *Atmospheric Research*, vol. 71, no. 1-2, pp. 3–34, 2004.

[20] D. Caro, W. Wobrock, and A. I. Flossmann, "A numerical study on the impact of hygroscopic seeding on the development of cloud particle spectra," *Journal of Applied Meteorology*, vol. 41, no. 3, pp. 333–350, 2002.

[21] W. A. Cooper, R. T. Bruintjes, and G. K. Mather, "Calculations pertaining to hygroscopic seeding with flares," *Journal of Applied Meteorology*, vol. 36, no. 11, pp. 1449–1469, 1997.

[22] N. Kuba and M. Murakami, "Effect of hygroscopic seeding on warm rain clouds - numerical study using a hybrid cloud microphysical model," *Atmospheric Chemistry and Physics*, vol. 10, no. 7, pp. 3335–3351, 2010.

[23] D. Rosenfeld and G. Gutman, "Retrieving microphysical properties near the tops of potential rain clouds by multispectral analysis of AVHRR data," *Atmospheric Research*, vol. 34, no. 1–4, pp. 259–283, 1994.

[24] C. G. Keyes Jr., G. W. Bomar, T. P. DeFelice, D. A. Griffith, and D. W. Langerud, *Guidelines for Cloud Seeding to Augment Precipitation*, American Society of Civil Engineers, Reston, VA, USA, 2016.

[25] D. K. Farmer, C. D. Cappa, and S. M. Kreidenweis, "Atmospheric processes and their controlling influence on cloud condensation nuclei activity," *Chemical Reviews*, vol. 115, no. 10, pp. 4199–4217, 2015.

[26] J. Rouquerol, F. Rouquerol, P. Llewellyn, G. Maurin, and K. S. Sing, *Adsorption by Powders and Porous Solids: Principles, Methodology and Applications*, Academic Press, Cambridge, MA, USA, 2nd edition, 2013.

[27] V. Bolis, C. Busco, M. Ciarletta et al., "Hydrophilic/hydrophobic features of TiO_2 nanoparticles as a function of crystal phase, surface area and coating, in relation to their potential toxicity in peripheral nervous system," *Journal of Colloid and Interface Science*, vol. 369, no. 1, pp. 28–39, 2012.

[28] H. Cheng and A. Selloni, "Hydroxide ions at the water/anatase TiO_2(101) interface: structure and electronic states from first principles molecular dynamics," *Langmuir*, vol. 26, no. 13, pp. 11518–11525, 2010.

[29] U. Aschauer, Y. He, H. Cheng, S.-C. Li, U. Diebold, and A. Selloni, "Influence of subsurface defects on the surface reactivity of TiO_2: water on anatase (101)," *The Journal of Physical Chemistry C*, vol. 114, no. 2, pp. 1278–1284, 2010.

[30] J. Goniakowski and M. J. Gillan, "The adsorption of H2O on TiO_2 and SnO_2(110) studied by first-principles calculations," *Surface Science*, vol. 350, no. 1-3, pp. 145–158, 1996.

[31] Ž. Knez and Z. Novak, "Adsorption of water vapor on silica, alumina, and their mixed oxide aerogels," *Journal of Chemical & Engineering Data*, vol. 46, no. 4, pp. 858–860, 2001.

[32] G. B. Alexader, "The effect of particle size on the solubility of amorphous silica in water," *The Journal of Physical Chemistry*, vol. 61, no. 11, pp. 1563-1564, 1957.

[33] G. B. Alexander, W. M. Heston, and R. K. Iler, "The solubility of amorphous silica in water," *The Journal of Physical Chemistry*, vol. 58, no. 6, pp. 453–455, 1954.

[34] V. Lenher and H. B. Merrill, "The solubility of silica," *Journal of the American Chemical Society*, vol. 39, no. 12, pp. 2630–2638, 1917.

[35] G. Okamoto, T. Okura, and K. Goto, "Properties of silica in water," *Geochimica et Cosmochimica Acta*, vol. 12, no. 1-2, pp. 123–132, 1957.

[36] J. D. Rimstidt and H. L. Barnes, "The kinetics of silica-water reactions," *Geochimica et Cosmochimica Acta*, vol. 44, no. 11, pp. 1683–1699, 1980.

[37] A. G. Tereshchenko, "Deliquescence: hygroscopicity of water-soluble crystalline solids," *Journal of Pharmaceutical Sciences*, vol. 104, no. 11, pp. 3639–3652, 2015.

[38] K. Hämeri, M. Väkevä, H.-C. Hansson, and A. Laaksonen, "Hygroscopic growth of ultrafine ammonium sulphate aerosol measured using an ultrafine tandem differential mobility analyzer," *Journal of Geophysical Research: Atmospheres*, vol. 105, no. D17, pp. 22231–22242, 2000.

[39] D. J. Cziczo, J. B. Nowak, J. H. Hu, and J. P. D. Abbatt, "Infrared spectroscopy of model tropospheric aerosols as a function of relative humidity: observation of deliquescence and crystallization," *Journal of Geophysical Research: Atmospheres*, vol. 102, no. D15, pp. 18843–18850, 1997.

[40] C. N. Cruz and S. N. Pandis, "Deliquescence and hygroscopic growth of mixed Inorganic–Organic atmospheric aerosol," *Environmental Science & Technology*, vol. 34, no. 20, pp. 4313–4319, 2000.

[41] I. N. Tang, "Phase transformation and growth of aerosol particles composed of mixed salts," *Journal of Aerosol Science*, vol. 7, no. 5, pp. 361–371, 1976.

[42] D. S. Covert, R. J. Charlson, and N. C. Ahlquist, "A study of the relationship of chemical composition and humidity to light scattering by aerosols," *Journal of Applied Meteorology*, vol. 11, no. 6, pp. 968–976, 1972.

[43] Y. Tai, H. Liang, A. Zaki et al., "Core/shell microstructure induced synergistic effect for efficient water-droplet formation and cloud-seeding application," *ACS Nano*, vol. 11, no. 12, pp. 12318–12325, 2017.

[44] K. Marbou, A. Al Ghaferi, and M. Jouiad, "In-situ characterization of Wettability alteration in Hopg," *SOP Transactions on Nanotechnology*, vol. 2374, pp. 1–10, 2015.

[45] N. Miljkovic, R. Enright, and E. N. Wang, "Effect of droplet morphology on growth dynamics and heat transfer during condensation on superhydrophobic nanostructured surfaces," *ACS Nano*, vol. 6, no. 2, pp. 1776–1785, 2012.

[46] C. Aprile, L. Maretti, M. Alvaro, J. C. Scaiano, and H. Garcia, "Long-lived (minutes) photoinduced charge separation in a structured periodic mesoporous titania containing 2,4,6-triphenylpyrylium as guest," *Dalton Transactions*, no. 40, pp. 5465–5470, 2008.

[47] Y. L. Du, Y. Deng, and M. S. Zhang, "Variable-temperature Raman scattering study on anatase titanium dioxide nanocrystals," *Journal of Physics and Chemistry of Solids*, vol. 67, no. 11, pp. 2405–2408, 2006.

[48] D. D. Do, *Adsorption Analysis: Equilibria and Kinetics*, Imperial College Press, London, UK, 1st edition, 1998.

[49] S. L. Clegg, K. S. Pitzer, and P. Brimblecombe, "Thermodynamics of multicomponent, miscible, ionic solutions "extended AIM aerosol thermodynamics model"," *The Journal of Physical Chemistry A*, vol. 96, no. , pp. 9470–9479, 1992.

[50] A. S. Wexler and S. L. Clegg, "Atmospheric aerosol models for systems including the ions H+, NH_4^+, Na^+, SO_4^{2-}, NO_3^-, Cl^-, Br^-, and H_2O," *Journal of Geophysical Research*, vol. 107, no. D14, 2002.

[51] E. Friese and A. Ebel, "Temperature dependent thermodynamic model of the system H^+–NH_4^+–Na^+–SO_4^{2-}–NO_3^-–Cl^-–H_2O," *The Journal of Physical Chemistry A*, vol. 114, no. 43, pp. 11595–11631, 2010.

[52] S. Ghorai, B. Wang, A. Tivanski, and A. Laskin, "Hygroscopic properties of internally mixed particles composed of NaCl and water-soluble organic acids," *Environmental Science & Technology*, vol. 48, no. 4, pp. 2234–2241, 2014.

[53] Y. Liu, Z. Yang, Y. Desyaterik, P. L. Gassman, H. Wang, and A. Laskin, "Hygroscopic behavior of substrate-deposited particles studied by micro-FT-IR spectroscopy and complementary methods of particle analysis," *Analytical Chemistry*, vol. 80, no. 3, pp. 633–642, 2008.

[54] C. Peng, B. Jing, Y.-C. Guo, Y.-H. Zhang, and M.-F. Ge, "Hygroscopic behavior of multicomponent aerosols involving NaCl and dicarboxylic acids," *The Journal of Physical Chemistry A*, vol. 120, no. 7, pp. 1029–1038, 2016.

[55] F. D. Pope, B. J. Dennis-Smither, P. T. Griffiths, S. L. Clegg, and R. A. Cox, "Studies of single aerosol particles containing malonic acid, glutaric acid, and their mixtures with sodium chloride. I. Hygroscopic growth," *The Journal of Physical Chemistry A*, vol. 114, no. 16, pp. 5335–5341, 2010.

[56] C. B. Richardson and T. D. Snyder, "A study of heterogeneous nucleation in aqueous solutions," *Langmuir*, vol. 10, no. 7, pp. 2462–2465, 1994.

[57] C.-P. Lin, H. Chen, A. Nakaruk, P. Koshy, and C. C. Sorrell, "Effect of annealing temperature on the photocatalytic activity of TiO_2 thin films," *Energy Procedia*, vol. 34, pp. 627–636, 2013.

[58] Q. Ma, H. He, and Y. Liu, "In situ DRIFTS study of hygroscopic behavior of mineral aerosol," *Journal of Environmental Sciences*, vol. 22, no. 4, pp. 555–560, 2010.

[59] Z. Mouline, K. Asai, Y. Daiko, S. Honda, S. Bernard, and Y. Iwamoto, "Amine-functionalized polycarbosilane hybrids for CO2-selective membranes," *Journal of the European Ceramic Society*, vol. 37, no. 16, pp. 5213–5221, 2017.

[60] G. E. Ewing and S. J. Peters, "Adsorption of water on NaCl," *Surface Review and Letters*, vol. 04, no. 04, pp. 757–770, 1997.

[61] B. Wassermann, S. Mirbt, J. Reif, J. C. Zink, and E. Matthias, "Clustered water adsorption on the NaCl (100) surface," *The Journal of Chemical Physics*, vol. 98, no. 12, pp. 10049–10060, 1993.

[62] D. D. Weis and G. E. Ewing, "Water content and morphology of sodium chloride aerosol particles," *Journal of Geophysical Research: Atmospheres*, vol. 104, no. D17, pp. 21275–21285, 1999.

[63] C. J. Walcek, "Cloud cover and its relationship to relative humidity during a springtime midlatitude cyclone," *Monthly Weather Review*, vol. 122, no. 6, pp. 1021–1035, 1994.

[64] R. T. Wetherald and S. Manabe, "An investigation of cloud cover change in response to thermal forcing," *Climatic Change*, vol. 8, no. 1, pp. 5–23, 1986.

[65] J. B. Condon, *Surface Area and Porosity Determinations by Physisorption: Measurements and Theory*, Elsevier, Amsterdam, Netherlands, 2006.

[66] K. S. W. Sing, "Reporting physisorption data for gas/solid systems with special reference to the determination of surface area and porosity (Provisional)," *Pure and Applied Chemistry*, vol. 54, no. 11, pp. 2201–2218, 1982.

[67] J. C. Callahan, G. W. Cleary, M. Elefant, G. Kaplan, T. Kensler, and R. A. Nash, "Equilibrium moisture content of pharmaceutical excipients," *Drug Development and Industrial Pharmacy*, vol. 8, no. 3, pp. 355–369, 1982.

[68] M. W. Scott, H. A. Lieberman, and F. S. Chow, "Pharmaceutical applications of the concept of equilibrium moisture contents," *Journal of Pharmaceutical Sciences*, vol. 52, no. 10, pp. 994–998, 1963.

[69] V. Murikipudi, P. Gupta, and V. Sihorkar, "Efficient throughput method for hygroscopicity classification of active and inactive pharmaceutical ingredients by water vapor sorption analysis," *Pharmaceutical Development and Technology*, vol. 18, no. 2, pp. 348–358, 2013.

[70] S. Patil, "A study of artificial rainfall," *International Journal of Multifaceted and Multilingual Studies*, vol. 3, 2016.

[71] E. Shotton and N. Harb, "The effect of humidity and temperature on the equilibrium moisture content of powders," *Journal of Pharmacy and Pharmacology*, vol. 17, no. 8, pp. 504–508, 1965.

[72] S. Builes, S. I. Sandler, and R. Xiong, "Isosteric heats of gas and liquid adsorption," *Langmuir*, vol. 29, no. 33, pp. 10416–10422, 2013.

[73] N. A. Aviara, O. O. Ajibola, and U. O. Dairo, "PH-postharvest technology," *Biosystems Engineering*, vol. 83, no. 4, pp. 423–431, 2002.

[74] A. H. Al-Muhtaseb, W. A. M. McMinn, and T. R. A. Magee, "Water sorption isotherms of starch powders," *Journal of Food Engineering*, vol. 61, no. 3, pp. 297–307, 2004.

[75] A. H. Al-Muhtaseb, W. A. M. McMinn, and T. R. A. Magee, "Water sorption isotherms of starch powders. Part 2: thermodynamic characteristics," *Journal of Food Engineering*, vol. 62, no. 2, pp. 135–142, 2004.

[76] S. Sircar, R. Mohr, C. Ristic, and M. B. Rao, "Isosteric heat of adsorption: theory and experiment," *The Journal of Physical Chemistry B*, vol. 103, no. 31, pp. 6539–6546, 1999.

[77] M. Yazdani, P. Sazandehchi, M. Azizi, and P. Ghobadi, "Moisture sorption isotherms and isosteric heat for pistachio," *European Food Research and Technology*, vol. 223, no. 5, pp. 577–584, 2006.

[78] M. Masuzawa and C. Sterling, "Gel-water relationships in hydrophilic polymers: thermodynamics of sorption of water vapor," *Journal of Applied Polymer Science*, vol. 12, no. 9, pp. 2023–2032, 1968.

[79] E. Tsami, "Net isosteric heat of sorption in dried fruits," *Journal of Food Engineering*, vol. 14, no. 4, pp. 327–335, 1991.